Edinburgh Research Explorer

Laser absorption spectroscopy for combustion diagnosis in reactive flows: A review

OPEN ACCESS
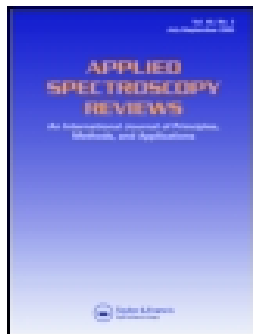
Laser absorption spectroscopy for combustion diagnosis in reactive flows: A review

Chang Liu & Lijun Xu

Published online: 13 Apr 2018.

Submit your article to this journal ☐

View related articles ☐

View Crossmark data ☐

Taylor & Francis
Taylor & Francis Group

Check for updates

Laser absorption spectroscopy for combustion diagnosis in reactive flows: A review

Chang Liu [iD][a] and Lijun Xu [iD][b]

[a]School of Engineering, The University of Edinburgh, Edinburgh, UK; [b]School of Instrument Science and Opto-Electronic Engineering, Beihang University, Beijing, China

ABSTRACT

Laser absorption spectroscopy (LAS) has been rapidly developed and widely applied to combustion diagnosis in recent decades. As a cost-effective tool for measuring multiple combustion parameters, LAS provides unique properties in terms of accuracy and sensitivity for understanding the reactions and kinetics in reactive flows. Line-of-sight and tomographic LAS techniques have stimulated numerous applications and been proved to be robust for *in situ* combustion diagnosis in uniform and non-uniform combustion fields, respectively. This review highlights the breakthroughs in the evolution of LAS techniques from the viewpoints of key principles, sensors and instrumentations developed for combustion diagnosis, with particular emphasis on a series of spatially-resolved LAS techniques with their recent applications on obtaining high-fidelity measurement results with minimal intrusion to the practical combustors. Along the way, we note some challenges and requirements for further development of the LAS-based combustion diagnosis.

Introduction

Combustion has been playing a significant role in producing thermal and kinetic energy from last century and is expected to be a main energy source for the next several decades. However, combustion emits pollutants inevitably, such as CO, NO_x and SO_x, which severely damage global environment and human health. In the technological aspects, various efforts have been made to minimize environmental disruption due to the combustion (1, 2). One aspect is adopting clean fuels, such as H_2 and CH_4, instead of coal and fossil fuels (3). Another and most important aspect is effectively utilizing the fuels and improving combustion efficiency (4). Therefore, flame characteristics such as temperature, multi-species concentrations and pressure are necessary to be monitored and used as feedbacks to actively adjust the combustion conditions in practical combustion processes.

In the recent decades, the non-intrusive laser spectroscopic techniques have been extensively applied to combustion diagnosis in reactive flows (5–10). Some representative

techniques mainly include laser absorption spectroscopy (LAS) (11–14), laser induced fluorescence (LIF) (15, 16), laser induced breakdown spectroscopy (LIBS) (17, 18), photoacoustic spectroscopy (PAS) (19, 20) and coherent anti-Stokes Raman scattering (CARS) (21–23). With respect to the target physical parameters and measurable dimensions illustrated in Table 1, each of these laser spectroscopic techniques has its superiority and feasibility to specific applications in the field of combustion research. To be specific, LAS is implemented by monitoring the absorbance while the laser wavelength is scanned over a certain spectral range for an absorbing species. Line-of-sight LAS has been validated to quantitatively measure the path-averaged temperature, species concentrations, pressure and velocity in the combustion fields (11). Spatially resolved 1D and 2D distributions of the parameters in the reacting flows are enabled by the combination of LAS and hard-field tomography (24). When the target species is excited by a laser beam, LIF is implemented by detection of the spontaneous emission of radiation, i.e. fluorescence, which is a measure of the population density of the target species (15). By forming the exciting laser beam into a sheet, a strong feature of easily imaging the 2D fluorescence intensity in the plane of the sheet makes LIF one of the most popular method, named as planar laser induced fluorescence (PLIF), for combustion diagnosis (25). By rapidly scanning a laser sheet across a flow field of interest, 3D LIF have been realized and applied to image droplet combustion and propellant combustion (26). However, quantitative measurement by PLIF is difficult due to the quenching effect that modifies the fluorescence intensity by depopulating the excited molecular states. LIBS is a powerful tool to measure the pointwise temperature and species concentration of very small-sized samples. For a typical LIBS experimental setup, a pulsed laser beam is focused to a spot on the sample and heats it to a very high temperature that breaks the sample into atoms and ions. When the atoms and ions re-combine, they emit an element-specific radiation that can be used to derive quantitatively the elemental composition in the measurement volume (17, 18). In addition, cold and hot gases are

Table 1. Comparison between representative laser spectroscopic techniques.

Spectroscopic techniques	Target physical parameters	Measurable dimensions	Available laser sources
LAS	• Temperature • Species concentration • Pressure • Velocity	• Path-averaged • 1D/2D (LAS tomography)	• Semiconductor lasers • HeNe laser
LIF	• Temperature, • Species concentration • Pressure • Velocity	• Pointwise • Path-averaged • 2D LIF (PLIF) • 3D LIF	• Nd:YAG laser • Argon-ion laser • Dye laser • CO_2 laser • Excimer laser
LIBS	• Temperature, • Species concentration	• Pointwise	• Nd:YAG laser • Ruby laser • CO_2 laser • N_2 laser • Excimer laser
PAS	• Species concentration • Aerosol	• Local (within the gas cell) • long range (with DPAS)	• Semiconductor lasers • CO_2 laser • HeNe laser
CARS	• Temperature, • Species concentration • Pressure • Velocity	• Pointwise • 2D	• Nd:YAG laser • Dye laser • ns/ps/fs-lasers

distinguished by the breakdown threshold, which is a function of the gas density (27). PAS is the measurement of the absorbed photon energy by means of its heat and hence the sound produced in the sample. The absorption of the modulated or pulsed radiation energy, represented by photons, produces heat in the sample. Therefore, the temperature changes periodically giving rise to a pressure wave, which is typically detected by a microphone or quartz tuning forks. The measurable dimensions with respect to PAS is typically limited in the gas cell that serves as a resonant cavity for sound waves (20). To realize long-range gas detection, the dynamic photoacoustic spectroscopy (DPAS) was developed by optical scanning large volumes of air (28). In addition, calibration is usually required for quantitative measurement by PAS due to the signal dependencies on hardware components (7). Using the resonant four-wave mixing, CARS has been proved to realize pointwise measurement of temperature, species concentration, pressure and velocity with high signal-to-noise ratios. The coherent laser signal employed by CARS leads to increase the sensitivity to trace quantities, but decrease the sensitivity to collisional quenching (21). By combining phase matching and detection schemes with the femtosecond excitation of Raman coherences, 2-dimensional CARS (2D-CARS) technique was proposed to realize planar temperature and chemical imaging (29). To categorize these laser spectroscopic techniques, the main limitation of LIBS is the lack of spatial resolution. Although DPAS can realize the spatially resolved gas monitoring, its temporal resolution is at a level of minutes that cannot meet the ms-level monitoring in turbulent combustion. PLIF and CARS require sophisticated and high-power laser sources and accurate alignments of the laser beams that are generally realized by elaborate optics layouts. As a result, the combustors should be significantly modified to achieve 2-axis or through optical accesses that withstand the pressure rise and temperature of the combustion process. These requirements often make LIF and CARS less applicable for *in situ* and real-time monitoring of practical combustors that are operated in harsh environments, e.g. with dust and strong mechanical vibration. LAS utilizes fiber optics to emit and collect thin pencil-beams in the region of interest. In this way, the optical windows can be made very small and discontinuous around the perimeter of the combustor, in any arrangement that complies with the operational requirement of the combustor (30). This gives rise to a significant superiority of LAS that the sensor can be embedded in practical combustors with minimal intrusions. Therefore, LAS is most promising to be applied to the combustion diagnosis of steel engines in the practical operating conditions (31).

As shown in Figure 1, gas molecules can be fingerprinted in the near- and mid-infrared bands using their absorption characteristics arising from rovibrational transitions and combination bands (32, 33). The general principle of LAS is to use these absorption
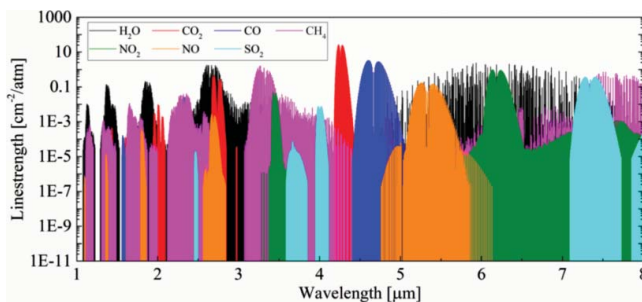

Figure 1. Fingerprinted gas molecules in the IR absorption spectrum at 1000 K.

characteristics for qualitative and quantitative gas analysis and identification. The concept of LAS was first introduced in 1970s and demonstrated to be feasible in measuring concentrations of IR-active species (34, 35). As an accurate, sensitive and fast-response optical modality, LAS exhibits significant advantages of measuring multiple combustion parameters, such as species concentrations, temperature, pressure, etc., *in situ* and in real time. From 1990s, the rapid technological advances of the room-temperature tunable laser sources have accelerated the development of LAS (36, 37). In this period, the tunable laser sources with different spectrum ranges, linewidths, output power and wavelength tuning ranges were invented and gradually became commercially available (38, 39). Typical types of the tunable laser sources employed in LAS mainly include near-infrared lasers, e.g. tunable diode lasers (TDLs) (40), vertical cavity surface emitting lasers (VCSELs) (41) and Fourier-domain mode-locked (FDML) lasers (42, 43), and mid-infrared lasers, e.g. interband cascade lasers (ICLs) (44, 45) and quantum cascade lasers (QCLs) (46, 47). Table 2 shows the main types and the corresponding features of the commercially available tunable laser sources. The parameters in the table are typical values for different types of laser sources. The laser sources could perform better with customized designs for specific applications. Nowadays, the tunable laser sources are compact, reliable and relatively cheap, and thus make LAS widely applied to combustion diagnosis in various areas, such as engines monitoring and design (43, 48–51), gas phase analysis in shock tubes (52–55) and power plant exhaust monitoring (56–58).

Targeting the combustion fields with different characteristics, a variety of LAS techniques have arisen in the recent decades. Line-of-sight LAS techniques, mainly classified as direct absorption spectroscopy (DAS) and wavelength modulation spectroscopy (WMS), were introduced to monitor combustion parameters that are constants or can be approximated as constants along the laser path (35, 59). To fulfill the increasing demand for monitoring non-uniform flow fields, LAS was further combined with 1- and 2-dimensional tomography sensors (24, 60, 61). In this way, spatially-resolved distributions of the combustion parameters can be successfully retrieved from the projections obtained by discrete laser beams from different views. This characteristic makes the LAS tomographic techniques most promising for *in situ* combustion diagnostics of engine and power plant where the measurement can only be implemented with limited optical accesses. Many efforts have been made from both the theoretical and experimental aspects to improve the reconstruction fidelity. Furthermore, novel sensors and instruments have been designed for reliable and accurate LAS measurements.

The applications of LAS have been reviewed by many researchers from different aspects. For instance, an earlier review by Allan elaborated the basic theory for LAS, typical sensor configurations and their applications in measurement of reactive flows and flame (13).

Table 2. Main features of typical types of tunable laser sources employed in LAS.

Laser types	Spectrum range	Linewidth	Output power	Wavelength tuning ranges
TDLs	~760 nm–3 μm	1–10 MHz	5–50 mW	1–3 cm^{-1}
VCSELs	650–1600 nm	1–30 MHz	0.5–5 mW	7–8 cm^{-1}
FDML lasers	1300–1550 nm	Order of GHz	3–100 mW	Up to 150 cm^{-1}
ICLs	2.9–6 μm	1–10 MHz	1–10 mW	Up to 20 cm^{-1}
QCLs	6–20 μm	1–5 MHz	1–500 mW	Up to 20 cm^{-1}

Martin reviewed the near-infrared diode laser sources and the specific techniques associated with LAS in chemical process and environmental air monitoring (62). Hanson *et al.* summarized the LAS strategies and sensors in shock tube diagnosis for studies of combustion chemistry (53). Bolshov *et al.* presented an overview of the state of the art of tunable diode laser-based sensors and their applications in measurements of temperature, species concentrations and pressure in harsh environments (63). Most recently, Goldenstein *et al.* not only thoroughly explained the underlying fundamentals of infrared LAS, but also documented the status of infrared LAS sensors and their roles in studying combustion science and characterizing the combustion-based systems (11). Cai *et al.* provided an extensive review of the mathematical foundations, experimental demonstration and practical application of tomographic absorption spectroscopy for the study of gas dynamics and reactive flows (24).

In this review, we aim at charting the milestones in the evolution of LAS from the viewpoints of key principles, sensors and instrumentations developed for combustion diagnosis. The review begins with introducing and particularly emphasizing the breakthroughs of line-of-sight (LOS) LAS techniques for measuring the uniform gas-dynamic properties over the past decades. Then, we mainly focus on a series of spatially-resolved LAS techniques with novel design of sensors and instrumentations, as well as with their most recent applications in diagnosing non-uniform flow fields. The review finally ends with a summary and a brief outlook for future development of the LAS techniques.

Line-of-sight LAS techniques

The line-of-sight (LOS) LAS techniques mainly target quantitative determination of the gas-dynamic properties for uniform combustion. According to the wavelength tuning schemes of the laser sources, the LOS LAS techniques are generally classified as DAS and WMS. Each scheme can be realized by either fixed- or scanned-wavelength approach. The fixed-wavelength approach is implemented by measuring the peak of the absorption lines, while the scanned-wavelength approach is realized by tuning the laser wavelength over the selected absorption transition. In general, the fixed-wavelength approach is able to provide an extremely high temporal resolution at a level of MHz, which is sometimes required for analyzing highly turbulent flows in the applications such as pulse detonation engines and shock tubes (64–66). However, the temperature and driving current of the tunable laser sources have to be precisely controlled to maintain the wavelength to the absorption peaks. In addition, two laser paths, with and without absorption, are required in the experiments if the collisional broadening effect of the spectrum is unknown. In contrast, the scanned-wavelength approach is more robust and accurate as it minimizes the impact of laser wavelength drift on the measurements. Therefore, this section reviews the key issues and significant advances with respect to scanned-wavelength DAS and WMS approaches.

Direct absorption spectroscopy (DAS)

As the most straightforward LAS technique, DAS was first introduced in early 1970s and have been successfully applied to combustion diagnosis during the recent decades (35). Nowadays, DAS is still widely used in many fields because of its irreplaceable advantages of easy implementation, free of calibration and high temporal resolution (49, 67–70). When a well collimated laser at central frequency v [cm^{-1}] enters a gas sample with a total path

length of L [cm], a proportion of light is absorbed and the wavelength-dependent transmission coefficient τ_v is described as

$$\tau_v = \left(\frac{I_t}{I_0}\right)_v = \exp\left(-P\int_0^L X_{abs}(x)S(T(x))\phi_v dl\right),\qquad(1)$$

where I_t and I_0 are the transmitted and incident laser intensities, respectively. P [atm] is the total pressure, $T(x)$ [K] the local temperature, $X(x)$ the local mole fraction of the absorbing species, ϕ_v [cm] the lineshape function and $S(T)$ [cm^{-2}atm^{-1}] the temperature-dependent line strength of the transition. Given a uniform flow field over the laser path, the absorbance α_v is defined as

$$\alpha_v = -\ln\left(\frac{I_t}{I_0}\right)_v = PX_{abs}S(T)\phi_v L.\qquad(2)$$

The scanned-wavelength DAS approach is implemented by acquiring the entire absorption feature through laser wavelength tuning over the target absorption transition. As shown in Figure 2, a polynomial baseline fit to the non-absorbing wings of transmitted laser intensity is first performed to extrapolate incident laser intensity in the absorbing frequency region (71). The absorbance is then acquired by taking the ratio between the incident and transmitted laser intensity.

Because the lineshape function ϕ_v is normalized so that $\int_{-\infty}^{+\infty}\phi_v dv \equiv 1$, the integrated absorbance area A of the transition, which is defined as the area underneath the absorption lineshape function, is given by

$$A = \int_{-\infty}^{\infty}\alpha_v dv = PX_{abs}S(T)L.\qquad(3)$$

Well known as the 2-color strategy, the ratio of the integrated absorbance areas at two transitions, noted as A_1 and A_2, can be expressed as a function of the path-averaged temperature in Eq. (4). Then, the partial pressure of the target gas, i.e. PX_{abs}, can be obtained from the integrated absorbance A_1 and the known $S_1(T)$:

$$R_{DAS} = \frac{A_1}{A_2} = \frac{PX_{abs}S_1(T)L}{PX_{abs}S_2(T)L} = \frac{S_1(T)}{S_2(T)}.\qquad(4)$$

The prerequisite of realizing scanned-wavelength DAS technique is obtaining the non-absorbing baseline. For the LAS measurements in engines applications, collisional broadening caused by high pressure make the determination of the non-absorbing baseline impossible (7). Furthermore, the nearby absorption lines may severely overlap with each other and cannot be decomposed even with the multi-peak Voigt lineshape fitting. Therefore, the DAS technique mainly targets the combustion fields with pressure generally lower than 1 atm.
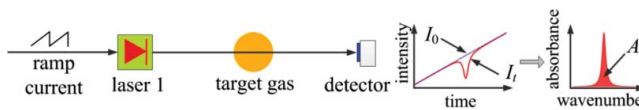

Figure 2. Schematic of the scanned-wavelength DAS.

Selection of absorption transitions and realization

One key point in the scanned-wavelength DAS technique is the appropriate selection of absorption transitions, which contributes to a better accuracy and sensitivity of the absorption measurement (72–76). With respect to the 2-color strategy, the line pair should be selected in consideration of moderate peak values of the absorbance, sufficiently different lower state energies E", and interference-free nearby transitions (73, 76). In general, the 2-color strategy is realized by two independent lasers using multiplexing schemes, e.g. time division multiplexing (TDM) and wavelength division multiplexing (WDM). Each of the lasers covers one transition of interest. With respect to the TDM scheme, the driving current of each laser is intermittently scanned by the ramp signal and set under the lower working threshold during a period (77, 78). As shown in Figure 3(a), the phase difference of the double-channel scanning signal is 180°. By combining the two lasers with a fiber-coupler, the absorption signals for the two transitions can be obtained by a photodiode detector. In contrast, the two lasers are scanned simultaneously and combined with the fiber-coupler for the WDM scheme. As shown in Figure 3(b), the transmitted lasers for the two transitions at different wavelengths are separated into different detectors after striking a grating (79, 80). Compare with the TDM scheme, WDM doubles the temporal resolution at the cost of one more detector. Furthermore, a significant improvement on the temperature sensitivity can be realized by scanning the wavelength over multiple absorption transitions. The broad spectral coverage facilitates the optimization of the sensitivity in different temperature ranges and used to be fitted against spectral databases for determination of combustion parameters (48, 81, 82).

Lineshape fitting and hardware implementation

In general, the raw absorbance is inevitably contaminated with background noise, which results in inaccurate calculation of the flow parameters from the integration of the raw absorbance. Therefore, a key procedure in the scanned-wavelength DAS approach is to reduce the negative influence background noise by fitting the Voigt lineshape of the absorption features. In general, influenced by the Gauss full width at half-maximum (FWHM) w_G and the Lorentz FWHM w_L, the Voigt lineshape function $\phi_V(v)$ is given by

$$\phi_V(v) = \frac{2}{w_G}\sqrt{\frac{\ln 2}{\pi}}\frac{a}{\pi}\int_{-\infty}^{+\infty}\frac{\exp(-y^2)}{a^2 + (w-y)^2}dy, \tag{5}$$

where

$$a = \sqrt{\ln 2}\frac{w_L}{w_G}, \quad w = \frac{2\sqrt{\ln 2}(v-v_0)}{w_G}, \quad y = \frac{2u\sqrt{\ln 2}}{w_G}. \tag{6}$$
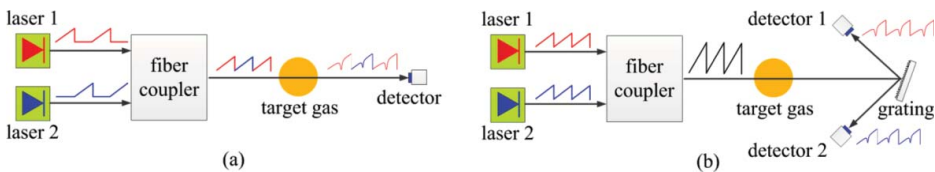

Figure 3. Realization of the 2-color DAS approach using (a) time division multiplexing and (b) wavelength division multiplexing.

As the analytic form of the Voigt function in Eq. (5) is unavailable, several numerical approaches were proposed to approximate the true Voigt function (83, 84). However, these numerical approaches are rather complicated and resources-consuming, which limits their applications in combustion scenarios with the requirements of measuring the flow parameters *in situ* and in real time. The Voigt parameter a describes the profile of the lineshape. It can be seen from Figure 4 that, when $a \geq 10$, the Voigt profile becomes a Lorentzian profile, while that becomes a Gaussian profile for $a \leq 0.01$. In case of $0.01 \leq a \leq 10$, each combination of a and w determines a point in the Voigt profile. Based on this approximation, Xu *et al.* demonstrated the high-precision on-line Voigt lineshape fitting for real-time scanned-wavelength DAS measurement in a system-on-chip (85). A look-up table, which depends on a and w, was established by taking the required accuracy of the DAS measurement into consideration, and the Voigt lineshape was rapidly and accurately calculated by the digital signal processor (DSP).

Wavelength modulation spectroscopy (WMS)

The background noise always contaminates the detector signal and becomes more significant in case of harsh environments with strong turbulent flows, mechanical vibrations and light scattering. At the cost of decreasing temporal resolution, some efforts seek to increase the signal to noise ratio by averaging the detector signal in a sequence of scanning periods (86, 87). Induced by beam steering and background light scattering, baseline fluctuation commonly exists in the whole measurement period, and thus invalidates the average-based attempts.

WMS is a sensitive and robust technique for measuring the combustion parameters with good noise-tolerant characteristics (88–90). As shown in Figure 5, the exciting current of the laser diode is generally driven by the superposition of a low frequency signal (ramp signal as an example) and a high frequency sinusoidal signal. The modulated laser frequency $v(t)$ can be expressed as

$$v(t) = \bar{v} + a\cos(2\pi f_m t), \tag{7}$$

where $\bar{v}$ is the scanning laser frequency, a and f_m the modulation amplitude and modulation frequency, respectively.
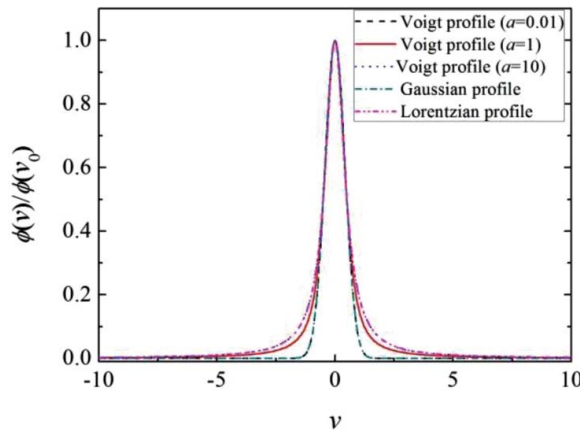

Figure 4. Comparison of normalized Voigt lineshape with normalized Gaussian and Lorentzian lineshapes. The figure has been reprinted with permission from Xu et al., 2014. Copyright © (2014) AIP Publishing (85).

The incident laser intensity $I(t)$ is modeled by

$$I(t) = \bar{I}_0[1 + i_1\cos(2\pi f_m t + \varphi_1) + i_2\cos(4\pi f_m t + \varphi_2)], \tag{8}$$

where $\bar{I}_0$ is the average laser intensity at center frequency $\bar{v}$, i_1 the amplitude of linear intensity modulation (IM), φ_1 the phase shift between the frequency modulation (FM) and IM, i_2 the amplitude of non-linear IM with phase shift φ_2 (91).

The transmission coefficient $\tau(v)$ becomes an even function in $2\pi f_m t$, which can be expanded into Fourier cosine series:

$$\tau(\bar{v} + a\cos(2\pi f_m t + \varphi)) = \sum_{n=0}^{n=+\infty} H_n(\bar{v}, a)\cos(n \cdot 2\pi f_m t), \tag{9}$$

where $H_n(\bar{v}, a)$ are the nth order harmonic coefficients given by

$$H_0(\bar{v}, a) = \frac{1}{2\pi} \int_{-\pi}^{+\pi} \tau(\bar{v} + a\cos\theta) \cdot d\theta, \tag{10}$$

$$H_n(\bar{v}, a) = \frac{1}{\pi} \int_{-\pi}^{+\pi} \tau(\bar{v} + a\cos\theta) \cdot \cos n\theta \cdot d\theta. \tag{11}$$

Followed by lock-in detection, the harmonics of the modulation frequency are extracted and used to infer the flow parameters. As the background noise is generally with relatively low frequencies, the WMS technique increases the signal to noise ratio to a large extent.

WMS-2f method

Reid and Labrie first introduced the concept of WMS and noted that the lineshapes of very weak absorption lines can be captured from the measurement of second-harmonic ($2f$) of the modulation frequency, known as the WMS-$2f$ method, without a zero-absorption baseline (59). This feature makes the WMS-$2f$ method robust for many realistic high-pressure combustors, in which the highly pressure-broadened lines increase the difficulty of accurate baseline fitting when using DAS approach.

By multiplying the detector signal with a sinusoidal reference signal at $2f_m$, the absolute magnitude of the second-harmonic of the modulated absorption signals, noted as R_{2f},
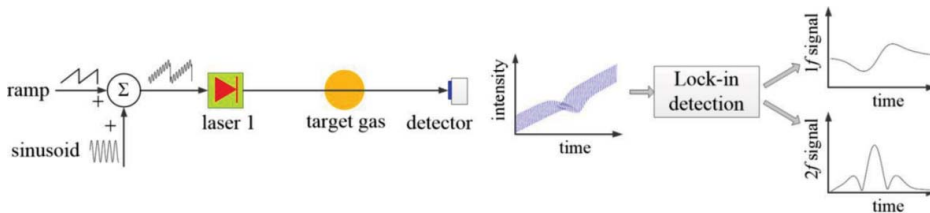

Figure 5. Schematic of the scanned-wavelength WMS.

isolated by the lock-in device is given by

$$R_{2f} = \sqrt{X_{2f}^2 + Y_{2f}^2}, \tag{12}$$

where X_{2f} and Y_{2f} are the X and Y components of the second-harmonic signals expressed by

$$X_{2f} = \frac{G\bar{I}_0}{2}\left[H_2 + \frac{i_1}{2}(H_1 + H_3)\cos\varphi_1 + i_2\left(H_0 + \frac{H_4}{2}\right)\cos\varphi_2\right], \tag{13}$$

$$Y_{2f} = -\frac{G\bar{I}_0}{2}\left[\frac{i_1}{2}(H_1 - H_3)\sin\varphi_1 + i_2\left(H_0 - \frac{H_4}{2}\right)\sin\varphi_2\right], \tag{14}$$

where G is the electro-optical gains of the detection system.

The magnitude of the absorption-based $2f$ signal, noted as S_{2f}, is calculated by

$$S_{2f} = \sqrt{(X_{2f} - X_{2f}^0)^2 + (Y_{2f} - Y_{2f}^0)^2}, \tag{15}$$

where X_{2f}^0 and Y_{2f}^0 represent the X and Y components of $2f$ signal without absorption.

For the small modulation depth, the laser intensity modulation can be neglected, i.e. $i_2 = 0$. If the phase shift between the FM and IM φ_1 is further assumed to be π, Eq. (15) becomes

$$S_{2f} = \frac{G\bar{I}_0}{2}\left|H_2 - \frac{i_1}{2}(H_1 + H_3)\right|. \tag{16}$$

Since H_1 and H_3 are odd functions, they are zero at the line center in the case of isolated and symmetric absorption features. The $2f$ peak height at the line center is free from the interference caused by the amplitude modulation distortions. For optically thin samples, generally $\alpha_v < 0.05$, the second-order harmonic coefficient can be simplified as

$$H_2(\bar{v}, a) = -\frac{PX_{abs}S(T)L}{\pi}\int_{-\pi}^{+\pi}\phi(\bar{v} + a\cos\theta)\cdot\cos2\theta\cdot d\theta. \tag{17}$$

As noted by Liu $et\ al.$, the gas temperature can be inferred from the ratios of $2f$ peak heights from two transitions, generally named as $2f$ peak ratio thermometry (92), as follows:

$$Ratio_{2f} = \frac{I_0(\bar{v}_1)H_2(\bar{v}_1)}{I_0(\bar{v}_2)H_2(\bar{v}_2)} = \frac{I_0(\bar{v}_1)S_1(T)\displaystyle\int_{-\pi}^{+\pi}\phi_1(\bar{v}_1 + a\cos\theta)\cdot\cos2\theta\cdot d\theta}{I_0(\bar{v}_2)S_2(T)\displaystyle\int_{-\pi}^{+\pi}\phi_2(\bar{v}_2 + a\cos\theta)\cdot\cos2\theta\cdot d\theta}. \tag{18}$$

Obviously, R_{2f} is not only a function of $S(T)$, but also a function of the line shape function ϕ that is modeled by the pressure and gas concentration. Therefore, the dependence of $Ratio_{2f}$ on the absolute temperature values should be calibrated based

on HITRAN/HITEMP spectral databases with measured pressure and a nominal expected value of gas concentration. In practice, WMS-2f method is more suitable to infer the temperature changes and flame fluctuations instead of calculating the absolute temperature values. More complicated calibration is needed for measuring gas concentration by scaling 2f signal units to the hardware-related parameter G (93). Furthermore, the optimum detection of broadened absorption spectra requires large modulation depths. Liu *et al.* provided a strategy to optimally select the modulation depth with highly broadened and congested spectra (94). However, the large modulation depths led to more pronounced non-ideal laser effects such as non-linear intensity modulation and FM/IM phase shift. In this case, absorption-based 2f signal S_{2f} cannot be simplified as Eq. (16), which, to some extent, invalidates the theory of 2f peak ratio thermometry.

Owing to the high SNR performance and high pressure applicability of the WMS-2f method, it has stimulated many practical applications since its invention. Philippe and Hanson determined the temperature and pressure of transient flows generated in a shock tube by fitting the experimental lineshapes to theoretical 2f lineshapes (95). In this study, velocity was also derived from the measurement of the Doppler shift of the absorption lines recorded with 2f detection. With a single laser that covers two adjacent oxygen transitions, Silver *et al.* employed the WMS-2f method for gas detection in microgravity (96). By detecting the 2f peak heights of H_2O transitions near 1.4 μm, Li *et al.* monitored the thermoacoustic instability and lean blowout of propane/air flames in a swirl-stabilized combustor (97).

Calibration-free WMS-2f/1f method
For WMS measurement in harsh environments, the difficulty of scaling 2f signal units to G is increased by the non-absorption transmission loss, which is caused by laser intensity fluctuations due to scattering, beam steering and window fouling. The solution is to normalize the 2f signal with first-harmonic (1f) signal, referred to as the calibration-free WMS-2f/1f method (91, 98, 99).

Using the same procedures as Eqs. (12)–(14), the magnitude of 1f signal can be calculated by

$$R_{1f} = \sqrt{X_{1f}^2 + Y_{1f}^2}, \tag{19}$$

where the components of 1f signal, X_{1f} and Y_{1f}, can be expressed by

$$X_{1f} = \frac{G\bar{I}_0}{2}\left[H_1 + i_1\left(H_0 + \frac{H_2}{2}\right)\cos\varphi_1 + \frac{i_2}{2}(H_1 + H_3)\cos\varphi_2\right], \tag{20}$$

$$Y_{1f} = -\frac{G\bar{I}_0}{2}\left[i_1\left(H_0 - \frac{H_2}{2}\right)\sin\varphi_1 + \frac{i_2}{2}(H_1 - H_3)\sin\varphi_2\right]. \tag{21}$$

As both the harmonics of the 2f and 1f signals are proportional to the hardware-related parameter G, the 1f-normalized 2f signal, noted as $S_{2f/1f}$, is independent of G and given by

$$S_{2f/1f} = \sqrt{\left[\left(\frac{X_{2f}}{R_{1f}}\right) - \left(\frac{X_{2f}^0}{R_{1f}^0}\right)\right]^2 + \left[\left(\frac{Y_{2f}}{R_{1f}}\right) - \left(\frac{Y_{2f}^0}{R_{1f}^0}\right)\right]^2}, \tag{22}$$

where R_{1f}^0 is the absorption-free 1f signal. In this way, the gas parameters can be directly obtained from the comparison between the simulations and measurements without scaling between the two. For optically thin samples ($\alpha_v < 0.05$), the peak value of $S_{2f/1f}$ obtained using small modulation depth can be simplified as

$$S_{2f/1f-\text{peak}} \approx \frac{PX_{abs}S(T)L}{i_1\pi} \int_{-\pi}^{+\pi} \phi(\bar{v} + a\cos\theta)\cdot\cos2\theta\cdot d\theta. \tag{23}$$

For optically thick conditions, simulations must be performed as close to the expected condition as possible due to breakdown of the linear approximation of Eq. (2). Iteration may be required to draw the simulations acceptably close to an unknown measurement condition (98). In addition, Peng *et al.* employed a second-order Taylor series to approximate laser transmission and measured the gas concentrations in case of $\alpha_v > 0.05$ (100). Lan *et al.* employed the ratios of the 2$^{\text{nd}}$ and 4$^{\text{th}}$ harmonics at the line center to measure the linewidth for optically thick conditions, which was applied in the WMS-2f/1f method to detect pressure and gas concentration (101).

At high-pressure conditions where absorption features are significantly broadened, over-modulation with modulation index $m > 2.2$ reduces the WMS-2f/1f measurement uncertainty induced by pressure deviation between the simulated and experimental conditions (102, 103). In case of large modulation index, the laser parameters, i.e. i_1, i_2, φ_1 and φ_2 in Eq. (8), are needed to be carefully characterized to obtain more accurate interpretation of the 1f-normalized 2f spectra. Following the general theory of Kluczynski and Axner (104), Li *et al.* extended the WMS model to account for real diode laser performance with the non-ideal laser effects, and demonstrated the extended model by probing pressure-broadened water vapor features near 1388 nm with a near-IR diode laser (91).

When compared with WMS-2f method, the calibration-free WMS-2f/1f method shows better applicability to monitor practical combustors where quantitative measurement of the gas properties is highly desired. Chao *et al.* demonstrated the WMS-2f/1f method for continuous monitoring CO in the boiler exhaust of a pulverized-coal-fired power plant up to temperatures of 700 K (57). Schultz *et al.* developed a sensor based on WMS-2f/1f method to measure temperature and H_2O column density in a hydrogen-fueled model scramjet combustor (54, 105). These quantitative and *in situ* measurements not only provide direct evidences of the suitability for WMS-2f/1f method in harsh environments, but also show great potential for optimization of the combustion efficiency in a combustor control system.

Fitting of the WMS-nf/1f method

Although calibration-free measurement of gas properties can be implemented by picking the peak value of the WMS-2f/1f signal, it may suffer from two disadvantages. First,

in case of large modulation depth and optically thick, simulations based on HITRAN must be performed close to the expected condition, which are difficult to be predicted in real conditions. Second, although the analytic model of laser intensity is characterized in Eq. (8), other optical components in the apparatus may produce uncertainties in the WMS background signals, and thus produce error in WMS-$2f/1f$ measurement results.

To mitigate the problems mentioned above, an innovative strategy, referred as fitting of the WMS-$nf/1f$ method, was developed by simulating the WMS-$nf/1f$ signals and fitting them to the measured ones (106–108). Figure 6 shows the flow chart of fitting the WMS-$nf/1f$. The basic steps of the method are listed as follows:

(1) By assuming v_0, A, w_G and w_L, the wavelength-dependent simulated absorbance $^S\alpha(v)$ can be obtained from Eq. (2) based on the HITRAN/HITEMP spectral database.

(2) The time-dependent simulated absorbance $^S\alpha(v(t))$ is obtained with the analytic expression for the laser wavelength versus time $v(t)$ in hand.
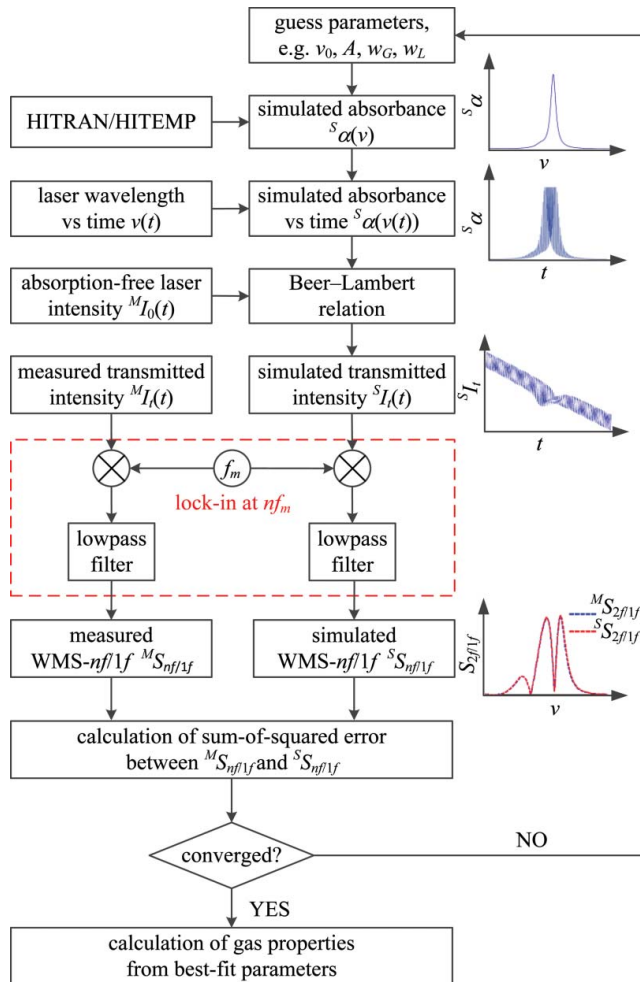

Figure 6. Flowchart of fitting the WMS-$nf/1f$ method.

Table 3. Comparison of scanned-wavelength LOS LAS techniques.

Sensing strategy	Benefits	Limitations
DAS	• Absolute measurement of *T* and *X* without calibration • Accurate for measuring strong absorbance • Ease of operation	• Invalid with broadened lineshape caused by high pressure and temperature • Low SNR for measuring weak absorbance ($\alpha_v < 5\%$)
WMS-2*f*	• Good noise-tolerant characteristics for measuring low absorbance[**] • Suitable for broadened lineshape in case of high pressure and temperature[**]	• Calibration needed to scale the simulations based on HITRAN/HITEMP databases to the measured 2*f* signal units • Careful selection of modulation depth in case of unknown pressure
CF-WMS-2*f*/1*f*	• Free of calibration for hardware-related parameters[*] • Resistant to laser transmission variations caused by beam-steering, scattering, etc.[*]	• Predetermination of the complex laser characteristics • Simulations must be performed close to the expected condition for optically thick conditions
Fitting of CF-WMS-*nf*/1*f*	• Avoiding the characterization of laser intensity in its response to scanning and modulating the injection-current • Valid at any optical depth, modulation index, and at all WMS-nf_m harmonics	• Absorption-free laser intensity versus time needs to be characterized

[**]Benefits for all the WMS methods.
[*]Benefits for CF-WMS-2*f*/1*f* and fitting of CF-WMS-*nf*/1*f*.

(3) The incident laser intensity $^{M}I_0(t)$ is measured in the absence of the absorption species. Given $^{M}I_0(t)$ and $^{S}\alpha(v(t))$, the simulated transmitted laser intensity $^{S}I_t(t)$ can be calculated by

$$^{S}I_t(t) = {}^{M}I_0(t) \cdot e^{-\alpha(v(t))} \tag{24}$$

(4) The laser penetrates the target species and the transmitted laser intensity $^{M}I_t(t)$ is measured.

(5) The digital lock-in and low-pass filter are used to obtain the 1*f* normalized *nf* signals of $^{S}I_t(t)$ and $^{M}I_t(t)$, noted as $^{S}S_{2f/1f}$ and $^{M}S_{2f/1f}$, respectively. By least-squares fitting $^{S}S_{2f/1f}$ to $^{M}S_{2f/1f}$, the parameters v_0, A, w_G and w_L can be obtained, from which the gas properties are finally inferred.

The use of $^{M}I_0(t)$ for simulation not only avoids characterizing the complex analytic model of laser intensity in its response to scanning and modulating the injection-current, but also accounts for any wavelength-dependent transmission of other optical components in the apparatus. Furthermore, the availability of this method with any optical depth and modulation index make it an attractive strategy for combustion diagnosis in harsh environments such as shock tubes (109), scramjet combustors (110, 111), detonation engines (50) and coal gasifiers (112–114). A comparison of various scanned-wavelength LOS LAS techniques is presented in Table 3 to clearly show their benefits and limitations.

Line-of-sight measurements in non-uniform conditions

Traditional LOS LAS techniques are typically employed to measure the path-averaged combustion parameters. However, non-uniform distributed characteristics of the combustion

fields extensively exist due to heat transfer with the side walls, cold boundary layers, and gas diffusion. Many researchers sought to evaluate the influences of the non-uniform field on the LOS measurements results. For instance, Ouyang and Varghese proposed an energy-temperature curve method to estimate the boundary-layer effects and chose absorption transitions to calculate absolute H_2O concentration (115). Wang *et al.* introduced a temperature-insensitive strategy to remotely acquire the CO concentration along the laser path with non-uniform temperature distribution (116). Smith *et al.* least-squares fitted the path-integrated scanned WMS-2*f*/1*f* spectrum to the simulated one to infer the integrated absorbance areas, by which the path-averaged temperature and H_2O mole fraction were calculated assuming a uniform line-of-sight measurement (117). Given two transitions with their line strengths linearly depending on the temperature over the domain of the temperature non-uniformity, Goldenstein *et al.* developed a 2-color absorption spectroscopy strategy for measuring the column density and density-weighted path-average temperature of the absorbing species in non-uniform gases (118). The ratio of integrated absorbance areas at two transitions was given by

$$R = \frac{m_2 \overline{T}_{n_i} + b_2}{m_1 \overline{T}_{n_i} + b_1}, \tag{25}$$

where m and b are constants that linearize $S(T)$ at each transition as

$$S_1(T) = m_1 T + b_1, \quad S_2(T) = m_2 T + b_2, \tag{26}$$

where n_i is the number density of the absorbing species. The density-weighted path-average temperature, $\overline{T}_{n_i}$, was defined as

$$\overline{T}_{n_i} \equiv \frac{\int_0^L T n_i dl}{\int_0^L n_i dl}. \tag{27}$$

With $\overline{T}_{n_i}$ in hand, the column density along the laser path in the non-uniform condition can be inferred from

$$N_i \equiv \int_0^L n_i dl = \frac{A}{S(\overline{T}_{n_i})}. \tag{28}$$

This strategy was validated and applied in the experiments with hypersonic propulsion facilities. Although above attempts took the non-uniform field into consideration, they were unable to acquire the spatially-resolved distributions of combustion parameters along the laser path.

By measuring multiple absorption transitions of a single species, the equation set that reflects the non-uniformity of the flow field can be established, by which the temperature probability distribution density can be extracted using the LOS LAS technique provided that

the partial pressure along the laser path can be regarded as a constant:

$$
\begin{bmatrix}
S_1(T_1) & S_1(T_2) & \cdots & S_1(T_n) \\
S_2(T_1) & S_2(T_2) & \cdots & S_2(T_n) \\
\vdots & \vdots & \vdots & \vdots \\
S_m(T_1) & S_m(T_2) & \cdots & S_m(T_n)
\end{bmatrix}
\cdot
\begin{bmatrix}
(PXL)_1 \\
(PXL)_2 \\
\vdots \\
(PXL)_n
\end{bmatrix}
=
\begin{bmatrix}
A_1 \\
A_2 \\
\vdots \\
A_m
\end{bmatrix}, \ (m > n) \qquad (29)
$$

To demonstrate this strategy, Sanders *et al.* reconstruct the temperature distribution of atmospheric-pressure air in 200–700 K with "two-value" and linear temperature distributed paths, respectively (119). Liu *et al.* retrieved two-value and parabolic-like temperature distribution based on multiple absorption transitions using temperature binning method. To some extent, these two attempts are able to acquire the temperature information with a relatively simple temperature profile (120). However, the general temperature profiles are not simply confined to two-value and parabolic-like cases. Meanwhile, the partial pressure cannot always be assumed to be a constant in practice. The spatially-resolved non-uniform distributions of the combustion parameters along the laser path can be measured when *a priori* information, such as the fitted profile function of the combustion field (121) and the temperature distribution tendency (122). The latter one provides a more general solution for retrieving the spatially-resolved flame parameters as the practical combustion fields cannot commonly described by fitting trapezoid or Boltzmann profiles. The temperature distribution tendency can be obtained through CFD simulation or several single-point thermocouple measurements. By equally dividing the measurement path into *n* sections, non-linear regularization method implemented by the simulated annealing algorithm can be employed to find an optimum solution of temperature distribution in Eq. (29). With the temperature distribution in hand, the partial pressure distribution can be retrieved by linear regularization methods.

One-dimensional LAS tomography

For some combustors such as the flat flame burner and the rocket propeller, the distributions of the combustion parameters over the cross-sections of the flame are rotationally symmetric, or, to some extent, can be simplified as rotationally symmetric (123, 124). In this case, LOS LAS measurements along arbitrary orientations are equivalent. By establishing Abel's integral equation, LOS LAS can be combined with 1-dimensional tomographic techniques (125), referred as 1-dimensional LAS tomography (1D-LAST) hereafter, to reconstruct the rotationally symmetric distributions of the combustion parameters.

As the Abel's integral equation is established by parallel projections, most 1D-LAST techniques were realized by using parallel-beam illuminations (96, 126–128). In general, a concentric circles-based model and a coordinate system are established, as shown in Figure 7(a). The origin of the coordinate system is at the center of the flame with radius R. The flame is discretized into N equal-spaced concentric circles. The interval of two adjacent concentric circles is $\Delta r = R/(N-0.5)$. The radius of the ith concentric circle is $r_i = i\Delta r$, $i = 1, \ldots, N$. As the flame is rotationally symmetric, the density of the integrated absorbance $a(r_i)$ in the ith

circle are uniform and can be expressed as

$$a(r_i) = P(r_i) \cdot S[T(r_i)] \cdot X(r_i). \tag{30}$$

N parallel laser beams, with interval Δr, penetrate the cross-section of the flame along the direction of positive y-axis. The coordinate of the intersection of the ith laser beam and x-axis is $x_i = i\Delta r$, $i = 1, \dots, N$. Therefore, the relationship between the integrated absorbance area $A(x_i)$ and $a(r_i)$ can be given by the Abel's integral equation:

$$A(x_i) = 2 \sum_{\substack{j=i}}^{N} \int_{\substack{r_j - \Delta r/2, j > i}}^{r_j + \Delta r/2} \frac{a(r_j)\tilde{r}}{\sqrt{\tilde{r}^2 - x_i^2}} d\tilde{r}, \tag{31}$$

where $a(r_i)$ can be solved by using 1-dimensional tomographic algorithms (125). By retrieving $a(r_i)$ at two transitions, the radial distributions of the combustion parameters can be obtained using the 2-color strategy.

Many previous works sought help from mechanical movements to achieve the parallel-beam illumination in the 1D-LAST system. Villarreal *et al.* set up a frequency-resolved 1D-LAST system by fixing the laser beam and attaching the burner on a translation stage. The burner moved into or out of the optical path to acquire parallel projection data (126). Instead of moving the burner, Guha *et al.* parallel swept the laser beam to the burner surface with a periscope mounted on a rotation stage and a single detector, both of which are positioned in the focal points of a pair of parabolic mirrors (128). The outstanding feature of above systems is the high spatial resolution, which is determined by the step distance of the movable stage. However, the structures of above 1D-LAST systems are rather complicated and difficult to realize on-line flame monitoring. To balance the system complexity and the spatial resolution, Liu *et al.* proposed a resolution-doubled 1D-LAST technique and sensor using one view of multiple parallel laser beams (129), as shown in Figure 7(b). With the designed geometry of the parallel laser beams, a doubled tomographic resolution of $\Delta r/2$ was realized when the interval of two neighboring parallel laser beams was Δr.
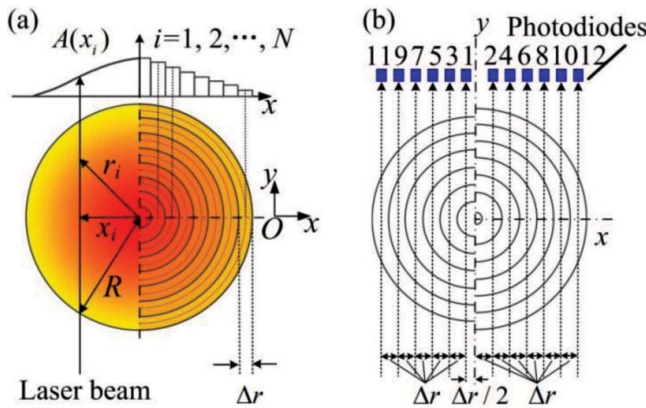

Figure 7. Illustration of (a) the parallel-beam geometry for 1D-LAST and (b) layout of the resolution-doubled 1D-LAST sensor. The figure has been reprinted with permission from Liu et al., 2015. Copyright © (2015) Springer Nature (129).

To realize the parallel-beam illumination, each laser beam is generally generated using a collimated lens. In contrast, the fan-beam illumination is much easier to generate using a well-collimated laser penetrates through a cylindrical lens. Therefore, to simplify the optics structure of the 1D-LAST system, the fan-beam illumination can be used instead of the parallel-beam illumination. The 1D-LAST system conceptually based on the fan-beam illumination was systematically introduced in (130). After transforming the fan-beam geometry to equivalent parallel-beam geometry with a 2-step interpolation (131), the rotationally symmetric distributions of temperature and gas concentration can be retrieved using 1-dimensional tomographic algorithms. Most recently, the fan-beam 1D-LAST system was employed to monitor swirling flames generated from a model swirl injector (132). As shown in Figure 8, the optical system was sufficiently simplified by introducing a fan-beam illumination and a linear detector array consisting 12 equally-spaced photodetectors. The thermal expansion over the cross-sections of interest in the swirling flame can be inferred from the reconstructed temperature profiles.

It is also worth mentioning that the stability of 1-dimensional tomographic algorithms largely depends on the spatial resolutions of the 1D-LAST sensors. As the Abel's integral equation is the first kind Volterra integral equation, it is inherently ill-posed and sensitive to noise-contaminated projection data (133). To achieve higher spatial resolutions, the target domain should be discretized into a larger number of concentric circles, i.e. unknown variables. The increasing number of unknown variables leads to a severely ill-posed problem, in which small perturbations on the projection data will be magnified and cause large errors on the reconstruction results. To treat these problems, regularization methods are good candidates. Daun *et al.* introduced a method based on Tikhonov regularization for solving the 1-dimensional tomographic problems for retrieving rotationally symmetric combustion parameters (127, 134). Hinging on choosing a suitable regularization parameter, Tikhonov regularization generates a well-posed problem that approximates the original ill-posed problem with a very small residual.

Two-dimensional LAS tomography

The increasing demands for monitoring more complicated and asymmetric combustion fields stimulate the development of 2-dimensional LAS tomographic techniques in the recent decade. From the mathematical formulation of the tomographic problems, the existed 2-dimensional LAS tomographic techniques can be generally classified as linear and non-linear LAS tomography, respectively. Based on a brief introduction of the model establishment, we mainly focus
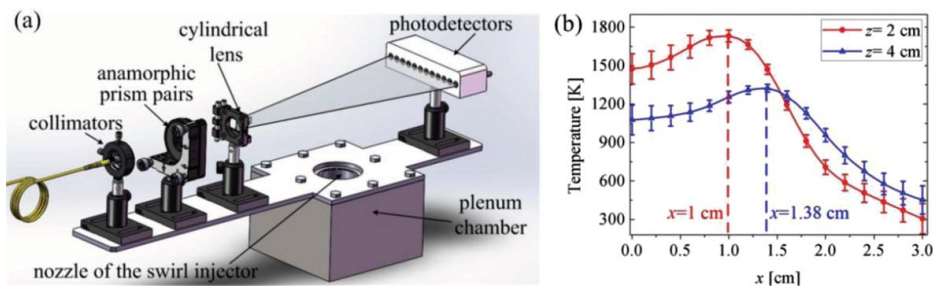

Figure 8. Application of the fan-beam 1D-LAST sensor on monitoring swirling flames. (a) shows the 3D sketch of the 1D-LAST sensor; (b) shows the reconstructed temperature profiles at different heights above the nozzle. The figure has been reprinted with permission from Liu et al., 2017. Copyright © (2017) IOP Publishing (132).

on the efforts made to improve the reconstruction fidelity and develop instrumentations aiming at realization of reliable and accurate measurements on practical combustors.

Linear LAS tomography

As indicated by its name, the linear LAS tomography is realized by solving the linear equation set, i.e. $\mathbf{Ax} = \mathbf{b}$, that forms the absorption-based tomographic problem (61). In principle, the mathematical formulation for linear LAS tomography is similar to the computer tomography that has been extensively employed in clinical diagnosis (131, 135). However, a complete and regular sampling used in the computer tomography is impractical for LAS tomography by taking the structure and reliability of the combustor into consideration. Both an efficient tomographic algorithm and a reasonable beam arrangement contribute to improving the quality of the tomographic images and thus making the linear LAS tomography competitive to be employed in on-line *and in situ* combustion diagnosis.

Model establishment

For the tomographic analysis, the region of interest (ROI) is discretized into N cells, as shown in Figure 9. In each cell, the flame parameters such as pressure P, temperature T and gas concentration X are assumed to be constant. According to Eq. (3), the sampled integrated absorbance $A_{v,i}$ obtained from the ith laser beam can be expressed as

$$A_{v,i} = \sum_{j=1}^{N} a_{v,j} L_{ij} = \sum_{j=1}^{N} [PS(T)X]_{v,j} L_{ij}, \tag{32}$$

where i and j are the indices of the laser beams and the grids, $a_{v,j}$ the density of the integrated absorbance in the jth grid, L_{ij} the absorption path length of the ith laser beam within the jth
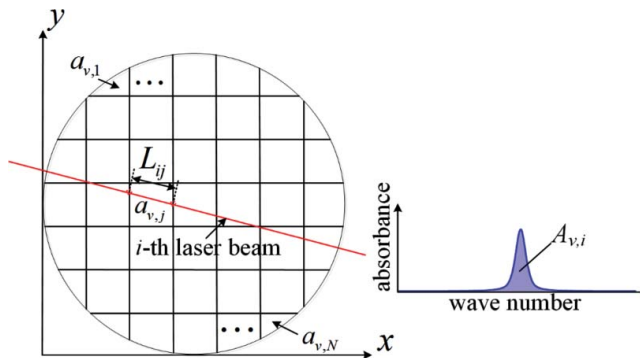

Figure 9. Geometric description of a line-of-sight LAS measurement in the linear LAS tomographic problem. The figure has been reprinted with permission from Liu et al., 2018. Copyright © (2018) IEEE (177).

grid. In general, Eq. (32) can be compactly rewritten as

$$\mathbf{Ax} = \mathbf{b}, \tag{33}$$

where $\mathbf{A}$ is the $M \times N$ matrix that represents the chord lengths of all the beams within each cell, $\mathbf{x}$ the $N \times 1$ vector of $a_{v,j}$ to be reconstructed and $\mathbf{b}$ the $M \times 1$ vector of sampled $A_{v,i}$, respectively. By performing the tomographic reconstruction at two pre-selected transitions, i.e. v_1 and v_2, the temperature T_j in the jth cell is reconstructed from the ratio of the reconstructed $a_{v_1,j}$ and $a_{v_2,j}$ in the jth cell using the 2-color strategy. Then, the partial pressure, i.e. $[PX]_{v,j}$, is calculated with T_j in hand.

In general, the quality of a tomographic image is evaluated by both the accuracy and spatial resolution (136). The former indicates the closeness of the tomographic image to the true one, while the latter refers to the fineness of the tomographic image. For linear LAS tomography, the quality of tomographic image can be improved mainly from two aspects, i.e. efficient tomographic algorithms and optimized layout of laser beams.

Tomographic algorithms

Depending on the numbers of ray measurements M and discretized cells N in the ROI, the linear LAS tomography gives rise to a "full-rank" or "deficient-rank" ill-posed problem shown in Figure 10 (137). The former case arises mainly in laboratory studies with high degrees of optical access when the axial and angular projection dimensions are densely sampled, that is, Eq. (33) is overdetermined due to the condition of Rank$(\mathbf{A}) \geq N$. In majority, the optical access is severely limited by taking the endurable high pressure and temperature of the combustor into account. Due to limited number of ray measurements, the linear LAS tomography gives rise to a rank-deficient problem, i.e. Rank$(\mathbf{A}) < N$.

Tomographic algorithms for treating full-rank but ill-posed problem. The filtered back-projection (FBP) algorithm that is commonly used based on the analytical solution of the Radon transform (138). Given a continuum of acquisition positions, the FBP reconstruction can be done by applying a row-wise convolution with a selectable kernel to the raw data. However,
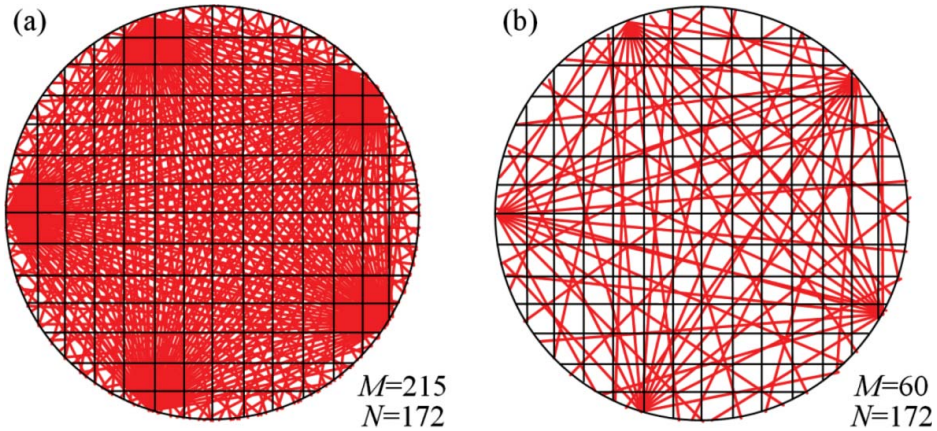

Figure 10. Beam density with respect to (a) full-rank and (b) deficient-rank ill-posed problems.

the FBP is less feasible in LAS tomography since complete and regular sampling is difficult to realize in practice (139). In contrast, algebraic reconstruction technique (ART) is more suitable for dealing with incomplete and irregular sampling (140–142), since ART uses multiple repetitions in which the current solution converges toward a better solution. As the simplest form of the iterative reconstruction algorithms, ART based on Kaczmarz' method is solved by (143)

$$\mathbf{x}^{k+1} = \mathbf{x}^k + \lambda \frac{\mathbf{b} - \mathbf{A}^T \mathbf{x}^k}{\|\mathbf{A}\|^2} \mathbf{A}, \tag{34}$$

where $\mathbf{x}^k$ is the reconstructed density of the integrated absorbance at the kth iteration, λ the relaxation parameter. When applying ART to an inverse problem with noise-contaminated data, the solution converges very quickly toward a good approximation of the exact solution, and begins to deviate due to its semi-convergence property. Therefore, the convergence should be monitored and a reliable stopping criterion is necessary for ART to stop the iterations at some point (144, 145). To achieve a faster convergence of volumetric images towards a stable solution, a variant of the ART, named as simultaneous ART (SART), performs updates for complete raw data projections (146). A relaxation factor is necessary in SART to keep the noise low and to reduce problems with streak artifacts. More applications of ART in the linear LAS tomographic measurements can be found in (144, 147–153).

Moreover, by using a singular value decomposition of the ill-conditioned matrix $\mathbf{A}$, we can obtain

$$\mathbf{A} = \mathbf{U}\mathbf{S}\mathbf{V}^T, \tag{35}$$

where $\mathbf{U} \in \mathbf{R}^{M \times M}$ and $\mathbf{V} \in \mathbf{R}^{N \times N}$ are orthonormal matrices, and $\mathbf{S} \in \mathbf{R}^{M \times N}$ is a diagonal matrix containing the singular values arranged in decreasing order, $\{\sigma_1, \sigma_2, \ldots, \sigma_N\}$. The least-squares solution of Eqn. (33) can be obtained by

$$\mathbf{x} = \sum_{j=1}^{N} \frac{\mathbf{u}_j^T \mathbf{b}}{\sigma_j} \mathbf{v}_j, \tag{36}$$

where $\mathbf{u}_j$ and $\mathbf{v}_j$ are the jth column vectors of $\mathbf{U}$ and $\mathbf{V}$, respectively. In practice, the ray measurements are contaminated with noise, in which case, $\mathbf{b} = \mathbf{b}^{\text{exact}} + \delta\mathbf{b}$, where $\mathbf{b}^{\text{exact}} = \mathbf{A}\mathbf{x}^{\text{exact}}$. Then, Eq. (36) can be written as

$$\mathbf{x} = \mathbf{x}^{\text{exact}} + \delta\mathbf{x} = \sum_{j=1}^{N} \frac{\mathbf{u}_j^T \mathbf{b}^{\text{exact}}}{\sigma_j} \mathbf{v}_j + \sum_{j=1}^{N} \frac{\mathbf{u}_j^T \delta\mathbf{b}}{\sigma_j} \mathbf{v}_j. \tag{37}$$

The small singular values amplify the second term of Eqn. (37). In other words, the solution suffers from a large variations using traditional constrained linear least-square method, even if smalls perturbation is added to the measurements, $\delta\mathbf{b}$. These problems can be suppressed by using regularization methods (154, 155), such as Truncated Singular Value Decomposition (TSVD) and standard Tikhonov regularization.

Tomographic algorithms for treating rank-deficient ill-posed problem. With respect to the tomographic algorithms for treating deficient-rank problem, the last *N-M* singular values in the orthonormal matrices are zero, and the physical solution of Eqn. (33) is given by

$$\mathbf{x} = \mathbf{x}^{LS} + \mathbf{x}^{null} = \sum_{j=1}^{M} \frac{\mathbf{u}_j^T \mathbf{b}}{\sigma_j} \mathbf{v}_j + \sum_{j=M+1}^{N} C_j \mathbf{v}_j. \tag{38}$$

where $\{C_j, j = M+1, \ldots, N\}$ are an underdetermined set of scalars. The exact solution $\mathbf{x}$ has two components: the unique solution $\mathbf{x}^{LS}$ belonging to the range of $\mathbf{A}$ that satisfies $\mathbf{Ax} = \mathbf{b}$, and an infinite set of solutions $\mathbf{x}^{null}$ from the null space of $\mathbf{A}$, $\mathbf{x}^{null} \in \{\mathbf{x} | \mathbf{Ax} = 0\}$. However, the "true" $\mathbf{x}^{null}$ cannot be retrieved from the ray measurements.

The limited ray measurements $\mathbf{b}$ must be supplemented with *a prior* information by taking the physical attributes of the target field into consideration. Many reconstruction techniques incorporate *a prior* information (sample-based or temporal prior information) through the Bayesian formulation (137, 156, 157). In general, *a prior* information such as smoothness of the subject and non-negativity constraint can be combined with the incomplete data to improve the image quality (158). The smoothing process provides the regularization necessary to render the inherently ill-posed problem tractable, while the non-negativity constraint maintains physically meaningful parameters. The first-order Tikhonov regularization spans the null space of $\mathbf{A}$ with a smoothing matrix $\mathbf{L}$, which approximates the directional derivatives (155, 158). For a Cartesian grid, $\mathbf{L}$ is defined as

$$\mathbf{L}_{ij} = \begin{cases} 1 & \text{if } i = j \\ -1/k & \text{if } i \text{ neighbours } j, \\ 0 & \text{otherwise} \end{cases} \tag{39}$$

and $\mathbf{Lx} = 0$ is satisfied by any uniform $\mathbf{x}$. Therefore, $\mathbf{x}$ can be resolved by

$$\mathbf{x}_\lambda = \text{argmin} \left\| \begin{bmatrix} \mathbf{A} \\ \lambda\mathbf{L} \end{bmatrix} \mathbf{x} - \begin{bmatrix} \mathbf{b} \\ 0 \end{bmatrix} \right\|, \quad s.t. \mathbf{x} \geq 0, \tag{40}$$

where the λ weighs the smoothness prior and the information contained in the ray measurements. It should be noted that the traditional λ selection method such as the L-curve criterion presumes the least-square solution is the correct with noise-free data (159), that is, $\mathbf{x}^{LS} = \mathbf{x}^{exact}$, which is not satisfied by the rank-deficient problem. Daun *et al.* introduced a λ selection method based on the singular value decomposition of the augmented matrix $[\mathbf{A}; \lambda\mathbf{L}]$ in Eq. (40), and further demonstrated its good solution accuracy in the rank-deficient problem (158).

In addition, the modified Landweber algorithm has been found robust in obtaining a stable solution of the inverse problem with limited views and a small number of ray measurements (60, 160). By taking the gradient of the least-squares objective function $\|\mathbf{Ax} - \mathbf{b}\|^2$

with respect to **x**, it is given in an iterative form as

$$\mathbf{x}^{k+1} = \mathbf{x}^k + \lambda_k \mathbf{A}^T (\mathbf{b} - \mathbf{A}\mathbf{x}^k), \tag{41}$$

The modified Landweber algorithm has gained widespread applications in linear LAS tomography by taking the smoothness of the subject and the value constraints into account (30, 161–165). A filter that uses a window of a specific size can be applied in order to regularize the solution and provide a degree of smoothing for obtaining an expected image resolution. By this mechanism, the estimate of each pixel value is determined by the value of the neighboring pixels within the filter window. The relaxation parameter plays an important role in obtaining an accurate and stable solution. Instead of using the training strategy to determine a fixed relaxation parameter, a "line search" strategy can be employed to compute the relaxation parameter in each iteration. It has been proved that the "line search" strategy is effective to make the solution to converge fast and improve the efficiency of the modified Landweber algorithm (166).

Beam optimization

For regular beam arrangements, i.e. parallel (58, 144, 161, 163, 167) and fan-shaped (150, 164, 168, 169) beam arrangements, the measurement space should be sampled evenly in spatial and angular dimensions to achieve the best image reconstruction results. Subject to the limits imposed by the physical size of the collimators and detectors, regular beam arrangements are often impractical in particular applications such as a multi-cylinder engine and a gas turbine engine (31, 170). To visualize the properties of any beam geometry, Terzija *et al.* first introduced sinogram space with one linear variable, *s*, and one angular variable, θ (162). As shown in Figure 11, each beam can be represented by a single point (s, θ) in the sinogram space, where *s* is the length of its
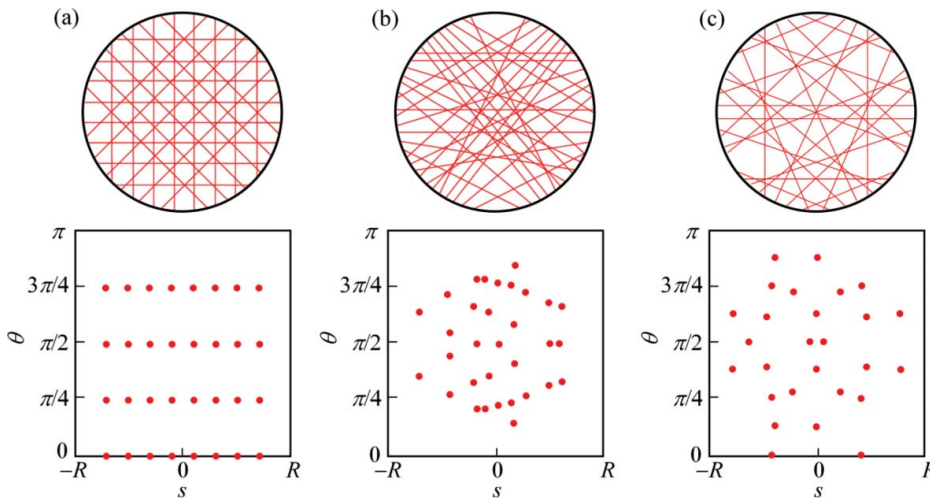

Figure 11. Beam arrangements and the corresponding sinogram plots. Beam arrangements are for (a) 32 beams with regular geometry, (b) 32 beams with unoptimized irregular geometry and (c) 27 beams with optimized irregular geometry. The figure has been adapted with permission from McCann et al., 2015. Copyright © (2015) Elsevier (61).

perpendicular distance from the origin when drawn in normal Cartesian coordinates and θ is the angle that it subtends to the vertical Cartesian axis. In this way, the sensitivity coverage of irregular beam arrangements can be inferred from plotting the positions of all the laser beams in the sinogram space. Laser beams that penetrate similar regions of physical space become repeated measurements of a single point in the sinogram space. Therefore, maximization of the discrepancy between these points would improve data gathering capability and thus the reconstruction accuracy.

Furthermore, a more systematic approach for predicting the performance of a beam arrangement was proposed based on the mathematical properties of the resolution matrix (171). The corresponding Euler equation for Eq. (33) is

$$\left(\mathbf{A}^T \mathbf{A} + \lambda \mathbf{L}^T \mathbf{L}\right) \mathbf{x} = \mathbf{A}^T \mathbf{b}, \tag{42}$$

and can be solved directly by

$$\mathbf{x}_\lambda = \left(\mathbf{A}^T \mathbf{A} + \lambda \mathbf{L}^T \mathbf{L}\right)^{-1} \mathbf{A}^T \mathbf{b} \equiv \mathbf{A}^\# \mathbf{b}. \tag{43}$$

If is separated into the exact and noise components, i.e. $\mathbf{b} = \mathbf{b}^{\text{exact}} + \delta \mathbf{b} = \mathbf{A} \mathbf{x}^{\text{exact}} + \delta \mathbf{b}$, Eq. (43) becomes

$$\mathbf{x}_\lambda = \mathbf{A}^\# \mathbf{A} \mathbf{x}^{\text{exact}} + \mathbf{A}^\# \delta \mathbf{b} = \mathbf{R} \mathbf{x}^{\text{exact}} + \mathbf{A}^\# \delta \mathbf{b}, \tag{44}$$

where $\mathbf{R} = \mathbf{A}^\# \mathbf{A}$ is the resolution matrix. The reconstruction error is defined by

$$\delta \mathbf{x} = \mathbf{x}_\lambda - \mathbf{x}^{\text{exact}} = (\mathbf{R} - \mathbf{I}) \mathbf{x}^{\text{exact}} + \mathbf{A}^\# \delta \mathbf{b}, \tag{45}$$

where $\mathbf{I}$ is the identity matrix. It can be seen that the reconstruction error is subject to the regularization error, i.e. $(\mathbf{R}-\mathbf{I})\mathbf{x}^{\text{exact}}$, and the error caused by perturbations in the data, i.e. $\mathbf{A}^\# \delta \mathbf{b}$, respectively. In tomographic problems with limited projections, $\delta \mathbf{x}$ is dominated by $(\mathbf{R}-\mathbf{I})\mathbf{x}^{\text{exact}}$ as the solution $\mathbf{x}_\lambda$ is robust to $\delta \mathbf{b}$ over a wide range of λ. That is to say, the beams should be arranged to minimize the Frobenius norm of $(\mathbf{R}-\mathbf{I})$ described by

$$F(\boldsymbol{\Psi}) = \|\mathbf{R}(\boldsymbol{\Psi}) - \mathbf{I}\|_F^2, \tag{46}$$

where $\boldsymbol{\Psi}$ contains the information of (s, θ) coordinates in the sinogram plot. Using a genetic algorithm, the beam arrangement can be optimized by solving

$$\boldsymbol{\Psi}^* = \arg \min[F(\boldsymbol{\Psi})]. \tag{47}$$

With respect to the above method, the resolution matrix is derived by incorporation of *a priori* information. When *a priori* information is not easily available, Yu *et al.* recently proposed a beam optimization method based on orthogonality between rows of the weight matrix $\mathbf{A}$ (172). The orthogonal degree (*OD*) between the ith and jth laser

beams is defined by

$$OD_{i,j} = \frac{\vec{A}_i \cdot \vec{A}_j}{\|\vec{A}_i\| \cdot \|\vec{A}_j\|}. \tag{48}$$

A zero value of $OD_{i,j}$ denotes the ith and jth laser beams are orthogonal, while the value of $OD_{i,j}$ is unity or close to unity means the two beams providing the same or very similar spatial information. A matrix containing the OD values of all beam pairs, named as MOD, is given by

$$MOD(\mathbf{\Psi}) = \begin{bmatrix} 1 & OD_{1,2} & \cdots & OD_{1,k} \\ OD_{2,1} & 1 & \cdots & OD_{2,k} \\ \vdots & \vdots & \ddots & \vdots \\ OD_{k,1} & OD_{k,2} & \cdots & OD_{k,k} \end{bmatrix}_{k \times k}. \tag{49}$$

To avoid redundant beams, every element in MOD should be small, which gives rise to the definition of the cost function for the minimization problem by

$$F_{MOD}(\mathbf{\Psi}) = \max[MOD(\mathbf{\Psi}) - \mathbf{I}], \tag{50}$$

where $\max[\cdot]$ returns the maximum element of the matrix. The minimization problem can be solved using a standard global optimizer such as the simulated annealing algorithm (173).

Design of tomographic sensors and systems

To obtain the ray measurements from different views, some previous implementations rely on beam scanning, e.g. either rotating the probing beams or translating the target (149, 150, 174). Figure 12 shows two representative implementation of the lab-scale LAS tomographic sensors based on beam scanning. To increase the temporal resolution of these tomographic system, Wang *et al.* captured the projections by simultaneously rotating four laser beams on the rotating platforms (149). However, the mechanical movements inevitably undermine the
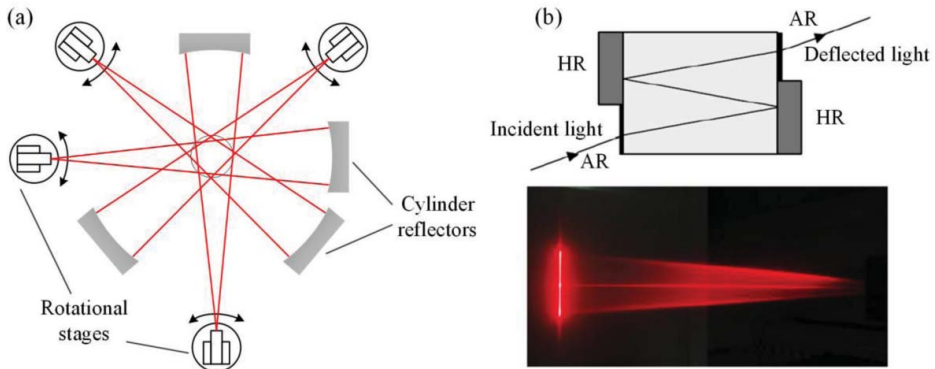

Figure 12. Schematics of two lab-scale LAS tomographic sensors implemented by (a) mechanical movements and (b) solid-state beam deflectors. The figure has been reprinted with permission from Tsekenis et al., 2017. Copyright © (2017) IEEE (175).
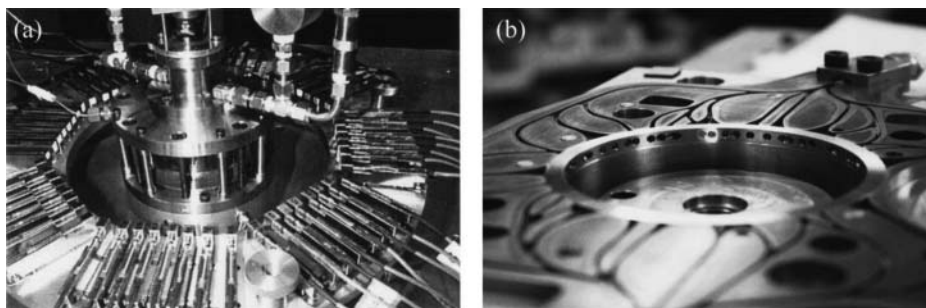
Figure 13. Implementation of the tomographic sensors with (a) 32 parallel laser beams. The figure has been reprinted with permission from Wright et al., 2005. Copyright © (2005) OSA Publishing (161) and (b) 27 irregular optical paths that were applied to combustion diagnosis in the multi-cylinder automotive engines. The figure has been reprinted with permission from Wright et al., 2010. Copyright © (2010) Elsevier (30).

temporal resolution which is also crucial for the monitoring of high speed flows. To rapidly scan the laser beam in the ROI without any mechanical movement, the solid-state beam deflectors were introduced recently to realize tomographic reconstruction with high temporal and spatial resolutions. The laser beam can be deflected with an angle of 216 mrad at a speed of 90 kHz using an electro-optic deflector (175). Combined with additional optical elements, different optical access strategies can be created based on the deflected laser beam.

The solutions for rank-deficient problems, such as the first-order Tikhonov regularization and modified Landweber algorithm, give rise to many linear LAS tomography measurements with limited number of laser beams (30, 161, 163–166, 169). Compared with the beam scanning manners, the stationary tomographic sensor not only enhances the temporal resolution, but also greatly reduces the uncertainty introduced by the beam movements and greatly improves the reliability. As shown in Figure 13, Wright *et al.* demonstrated high-speed tomographic imaging of hydrocarbon vapor distribution and mixing within the combustion chamber with 32 parallel laser beams (161, 176) and 27 irregular optical paths (30), respectively. These sensors were applied to combustion diagnosis in the multi-cylinder automotive engines to understand the mixing and reaction processes. Particularly, the sensor with 27 optical paths carried optical fibers and collimators embedded on a unique Optical Access Layer (OPAL), which offered minimal modification of engine form and function.

As shown in Figure 14, Liu *et al.* developed a fan-beam LAS tomographic sensor with 60 projections and simultaneously reconstructed the 2-dimensional distributions of temperature and H_2O concentration with a high spatial resolution of 7.8 mm (164). Most recently, the newly developed highly spatially-resolved sensor was employed to monitor the dynamic cross-sectional behavior of swirling flames. Particularly, the developed sensor was applied to capture dynamically the process of blowout of the swirling flame, illustrating that the sensor can provide firsthand and reliable visual data to help prevent the flame from lean-blowout (177).

Image reconstruction with limited number of laser beams makes the parallel data acquisition (DAQ) system easier to be implemented in practical applications, and, therefore, the high temporally-resolved LAS tomographic system becomes a reality. A parallel high-speed DAQ for LAS tomography can be established in two main approaches, i.e. assembly of commercial instruments and custom-made compact reconfigurable instruments. In most cases,
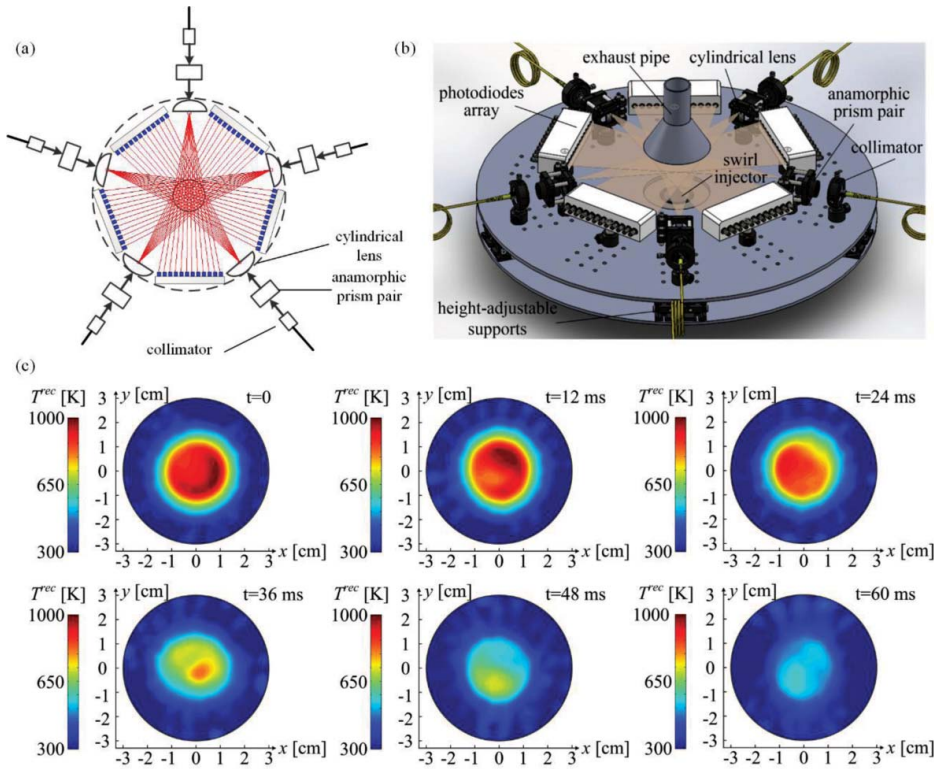
Figure 14. Stationary fan-beam LAS tomographic sensor with its applications on monitoring the dynamic cross-sectional behavior of swirling flames. (a) Schematics of the fan-beam sensor with 60 projections. (b) Installation of the sensor above the nozzle of the model swirl injector. (c) Instantaneous tomographic images of temperature over the cross-section of the swirling flame at a height of 2 cm above the nozzle during the blowout event. The figure has been reprinted with permission from Liu et al., 2018. Copyright © (2018) IEEE (177).
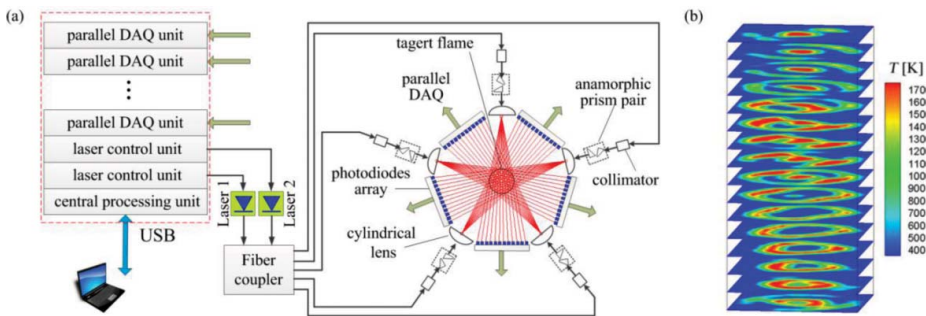
Figure 15. LAS tomographic system based on the stationary fan-beam tomographic sensor and parallel DAQ units. (a) Functional diagram of the electronic circuits. (b) 2D temperature distributions of an impulse flame generated by a Bunsen burner at 8 kfps. The figure has been reprinted with permission from Jing et al., 2017. Copyright © (2017) IEEE (179).

the commercial DAQ units were adopted. For instance, a 16-laser-beam LAS tomography system was developed with HIOKI commercial instruments that enable to generate 1k frames of tomographic images per second (178). The National Instruments digital DAQ cards were used to parallel sample the absorption signal with respect to the OPAL (30). Recently, parallel DAQ units with memory chips were recently designed to collect 60 channels of absorption light intensity data (179). As shown in Figure 15, compact and integrated electronic circuits that contain a central processing unit, laser control units, and parallel DAQ units were developed with a shared-bus interconnection. Based on the stationary fan-beam LAS tomographic sensor, the temporal resolution of fan-beam LAS tomographic system was reconfigurable from 1k to 8k frame per second (fps).

Non-linear LAS tomography

Motivated by the advancements in broadband laser sources and related wavelength-multiplexing technologies, the non-linear LAS tomographic methods were proposed by rapidly obtaining absorption information over a wide spectral range (180). The central idea is to increase the spectral sampling through broadband wavelength sweeping so that the deficiencies in spatial sampling can be alleviated. As introduced previously, the linear LAS tomography reconstructs the distributions of absorbance for individual transitions, which are linearly related to the ray measurements from multiple views and used to further infer the distributions of combustion parameters. Different from the linear LAS tomography, the non-linear LAS tomography achieves that directly by solving a set of non-linear equations with these parameters involved.

Model establishment

The physical and mathematical background of the non-linear LAS tomographic techniques has been detailed in (24, 181–183). Here, we provide a brief summary of the physics and mathematics to facilitate the discussion in the rest of the paper. Figure 16 shows the mathematical formulation of the hyperspectral tomography (HT) problem. A jth laser beam with tunable wavelengths covering multiple transitions penetrates the ROI with absorbing species, and results in a projection spectrum, i.e. the absorbance $p(l_j, \lambda)$ with λ indicating the swept wavelength. That is to say, the absorbance at a certain wavelength, e.g. λ_i, contains contributions not only from λ_i itself, but also from the other transitions centered at different
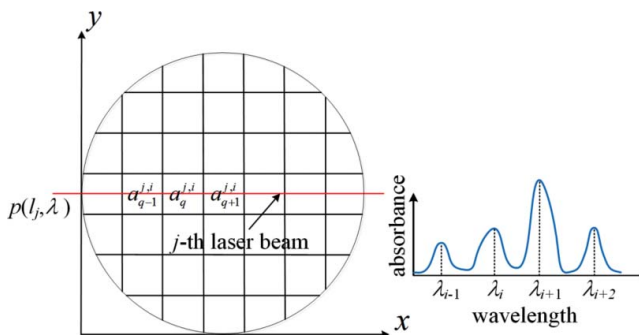

Figure 16. The mathematical formulation of the hyperspectral tomography problem. The figure has been adapted with permission from Ma et al., 2009. Copyright © (2009) OSA Publishing (180).

wavelength, e.g. λ_{i-1}, λ_{i+1} and λ_{i+2}. The peak of the absorbance at λ_i is expressed by

$$p(l_j, \lambda_i) = \sum_q a_q^{j,i}(T_q, X_q, P_q) = \sum_q \sum_k S(\lambda_k, T_q) \cdot X_q \cdot \phi(\lambda_k - \lambda_i, T_q, X_q, P_q) \cdot P_q \cdot \Delta, \quad (51)$$

where q is the index of the cell penetrated by the jth laser beam. $a_q^{j,i}$ is the absorbance in the qth cell at λ_i. T_q, X_q and P_q are the temperature, concentration and pressure in the qth cell, respectively. λ_k is the center wavelength of the kth contributing transition. Δ is the cell spacing.

This inverse problem of reconstructing T_q, X_q and P_q is cast into an algebraic non-linear minimization problem with a cost function defined as

$$D(T_q, X_q, P_q) = \sum_{j=1}^{J} \sum_{i=1}^{I} \left[1 - p_c(l_j, \lambda_i, T_q, X_q, P_q)/p_m(l_j, \lambda_i) \right]^2, \quad (52)$$

where J and I represent the total number of laser beams and the peak wavelengths, respectively. $p_m(l_j, \lambda_i)$ is the measured projection for the jth laser beam at λ_i, while $p_c(l_j, \lambda_i, T_q, X_q, P_q)$ is the computed projection based on reconstructed T_q, X_q and P_q. It can be seen that the function D represents the closeness between the reconstructed and actual distributions of temperature, concentration and pressure. The reconstructed distributions are sought to minimize the difference between the projections computed based on them and the measured projections.

As the linear LAS tomography relies on the integrated line-of-sight measurements, only the DAS can be incorporated in the tomographic techniques. Although WMS is superior to DAS with respect to sensitivity and noise resistance, it is inapplicable for the linear LAS tomography due to its non-linear nature based on harmonic detection. Non-linear LAS tomography creates an irreplaceable advantage by combining WMS theory and facilitates the application in harsh environments (184). The WMS-$2f/1f$ signal from the transitions with different temperature dependence can be incorporated in the non-linear LAS tomographic problem, from which the temperature, species concentrations and pressure can be directly modeled. In this case, the cost function D is given by

$$D(T_q, X_q, P_q) = \sum_{j=1}^{J} \sum_{i=1}^{I} \left[1 - S_{2f/1f}^c(l_j, \lambda_i, T_q, X_q, P_q)/S_{2f/1f}^m(l_j, \lambda_i) \right]^2, \quad (53)$$

where $S_{2f/1f}^c$ and $S_{2f/1f}^m$ are the calculated and measured $1f$-normalized $2f$ signals, respectively.

To alleviate the ill-posed nature of this non-linear optimization problem, regularization is also applied to the minimization problem by characterizing the smooth distributions of combustion parameters in the gas flow. With respect to the smoothness regularization, the cost function can be modified as

$$F = D(T_q, X_q, P_q) + \gamma_T \cdot R_T(T_q) + \gamma_X \cdot R_X(X_q) + \gamma_P \cdot R_P(P_q), \quad (54)$$

where R_T, R_X and R_P are the smoothness regularization factors, γ_T, γ_X and γ_P are weighting
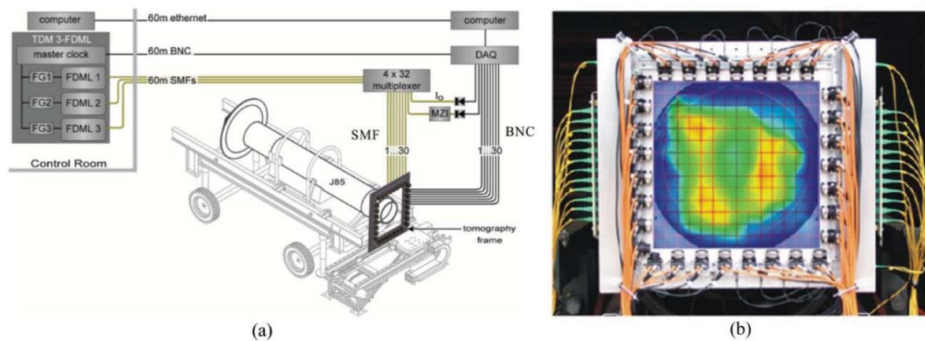
Figure 17. Application of the HT sensor at the exhaust stream of a J85 engine. (a) Overview of the experimental setup with a 30-beam HT sensor. (b) Photograph of the optical test section hardware overlaid by a sample tomographic reconstruction to illustrate the location of the flow field. The figure has been reprinted with permission from Ma et al., 2013. Copyright © (2013) OSA Publishing (187).

parameters employed to scale the magnitudes of R_T, R_X and R_P, respectively. More details on determining the optimal regularization parameters in the non-linear LAS tomography can be found in (185). Therefore, the non-linear LAS tomography problem is described by a combination of the closeness between the reconstructed and the actual distributions and the smoothness regularization factors. The simulated annealing algorithm (SA) has been proved to be suitable for the optimization of the non-linear LAS tomography problem (173). As detailed in (186), some variants of the SA algorithm were also proposed to reduce the computational cost.

System design and applications
The first experimental demonstration of the non-linear LAS tomography was carried out by using a prototype sensor on a near-adiabatic, atmospheric-pressure laboratorial Hencken burner (180). The temperature and H_2O concentration in seven discretized zones of the Hencken burner were reconstructed using six fiber-coupled laser beams, which were generated using a fiber Fabry–Perot tunable filter laser with wavelength tuning over 1333–1377 nm at a repetition rate of 200 Hz. Up to now, the most representative application of the non-linear LAS tomography is the combustion diagnosis of an aero-propulsion engine (General Electric J85) shown in Figure 17 (187). With a time-division-multiplexed combination of three FDML laser sources, the output laser can sweep over 10 cm^{-1} at a repetition rate of 50 kHz. The laser system, labeled as TDM 3-FDML in Figure 17, was operated from the facility control room and 60-m-long optical fibers were used to transmit the laser to the engine location. A 4×32 multiplexer located near the engine was used to combine and split the three laser signals into 32 independent outputs. A customer-built tomography frame with 15 horizontal and 15 vertical laser beams was mounted at the exit plane of the exhaust nozzle. With a 36.3 mm beam spacing, the 2-dimensional distributions of temperature and H_2O concentration were simultaneously reconstructed with a temporal resolution of 50 kHz at 225 spatial grid points.

Discussions
The non-linear LAS tomography is superior to the linear LAS in three main aspects. First, the number of projections can be reduced due to the availability of absorption information

at multiple wavelengths. This essential advantage makes the non-linear LAS tomography more attracting for application in combustors with limited optical access. Second, employment of broadband frequency-agile laser sources contributes to a high-repetition-rate wavelength sweep, and thus a high temporal resolution, which facilitates tomographic measurements in the combustion fields with strong turbulence. Third, the non-linear LAS tomography maintains good sensitivity in a wide range of temperature with appropriate selection of multiple transitions, and thus makes the inverse problem more stable and insensitive to measurement noises.

Although non-linear LAS tomography has many advantages, it is less competitive than linear LAS tomography in the aspects of system realizability and real-time performance. Compared with the linear LAS tomographic system that requires generally narrowband laser diodes with a tunable frequency range $1\text{--}2$ cm^{-1} and a photodiode detector with a moderate bandwidth, e.g. 10–50 MHz, the non-linear LAS tomographic system requires expensive broadband light sources and large-bandwidth photodiode detectors to sample numerous absorption features with a high repetition rate. For instance, the laser output from a supercontinuum laser source with an ultra-high repetition rate on the order of MHz requires the bandwidth of the photodiode detector up to 10 GHz (188, 189). A higher bandwidth of the photodiode detector leads to a smaller active area and thus reduces the efficiency of the laser sources. In addition, complex calculations are needed to fit broadband absorption spectra when implementing the non-linear LAS tomography (190), which are far beyond the handling capacity of a system-on-chip and should be carried out off-line using a more powerful computer. It is impractical to employ a non-linear LAS tomography in combustion scenarios such as thermal power plants and incinerator facilities, in which the combustion processes are highly demanded to be observed in real time and adjusted actively. A comparison of linear and non-linear LAS tomographic techniques in the aspects of theory and system implementation is shown in Table 4.

Last but not least, parallel laser beams with orthogonal views were used for image reconstruction in many non-linear LAS tomographic methods. The maximum number of grids equals to the multiplication by the numbers of horizontal and vertical laser beams. Indeed, employment of the multiple transitions contributes to a larger number of projections, which, to some extent, alleviates the deficiencies in spatial sampling. However, the measurement accuracy can be hardly improved with even larger number of transitions if the optimal transitions for a given temperature range have already been included (191). In this case, additional spatial samples from other angular views or more beam arrangements are necessary to further improve the quality of the tomographic image.

Summary and outlook

Combustion diagnosis plays an important role in better understanding the thermal processes and improving the combustion efficiency. LAS has been proved to be a reliable, accurate, sensitive and fast-response optical modality for combustion diagnosis. The rapid technological advances of small-size and narrow-linewidth tunable laser sources accelerate the development of LAS techniques in the recent decades. Nowadays, commercially available tunable laser sources can cover a wide spectral range, which provide LAS measurements with higher sensitivity for combustion-like temperature

Table 4. Comparison of linear and non-linear LAS tomographic techniques.

Aspects	Characteristics	Linear LAS tomography	Non-linear LAS tomography
Theory	Number of transitions	One or two	Multiple, depending on the number of grids
	Beam arrangements	At least three views in different spatial and angular dimensions	At least two with orthogonal views
	Tomographic algorithms	Iterative reconstruction algorithms and regularization methods	Algebraic non-linear minimization with regularization
	Temperature sensitivity	Moderate temperature sensitivity regarding the E'' of the selected two transitions	Good temperature sensitivity in a wide temperature range
	Incorporation with WMS	Invalid	Valid
	Computational cost	Low	High
System implementation	Laser sources	Room-temperature and small-size TDLs	Broadband frequency-agile lasers
	Photodiode detector	Moderate bandwidth, e.g. 10–50 MHz	High bandwidth, e.g. hundreds MHz and even order of GHz
	Ease of tomographic sensor design	Complicated, careful consideration of beam arrangements required	Relatively simple with orthogonal views
	Availability of real-time measurement	Achieved by a system-on-chip	Hard to be realized due to the complex calculations

measurement and lower lower-limit of concentration measurement. This review presented the development of LAS from the viewpoints of techniques, sensors and instrumentations when applied to combustion diagnosis.

LOS LAS techniques have been widely employed to monitor the uniform combustion fields when the parameters along the laser path are constants or can be approximated as constants. DAS can be easily implemented to measure absolute flame parameters with relative low pressure. In a harsh environment with elevated pressure and strong turbulence, WMS techniques show good noise-tolerant characteristics for measuring low absorbance. For practical combustors such as shock tubes, pulse denotation engines and scramjet combustors, LOS LAS sensors present good reliability for *in situ* combustion diagnosis.

To satisfy the increasing demands for measurements in complicate and turbulent flow fields, the LAS techniques gradually evolve from the path-averaged to spatially-resolved measurement. Along the way, novel sensors and instrumentations have been designed to increase the accuracy and suitability of the LAS techniques for practical applications. LOS measurements with multiple transitions reflect the non-uniform information of a combustion fields along the laser path. One-dimensional LAS tomography is capable of monitoring rotationally symmetric flames. Particularly, the most promising results have been obtained by 2-dimensional LAS tomography in reconstruction of the non-uniform distributions of combustion parameters.

For a better understanding of the combustion processes, it is necessary to measure more species among the combustion intermediates and products in the future research. Therefore, a deeper exploration on the spectroscopic database will be required to obtain accurate distributions of parameters for these species. In addition, developments in fundamental optics and optical engineering will improve the performance of laser sources, particularly the mid-infrared laser sources, in many aspects such as high-power laser output, high stability in wavelength tuning and multi-wavelength coverage, etc. Regarding the state-of-the-art in the LAS tomography, future analytical model should be established to evaluate the dependence of the reconstruction fidelity on the intensiveness of sampled transitions and effectiveness of beam arrangement. Furthermore, solutions will be customized to design the tomographic sensors with suitable spatial and temporal resolutions for the targeted combustors. Under the operating conditions of elevated temperature and pressure, many efforts should be made to focus on maintaining the stability of the combustors by appropriate tomographic sensor design with minimal intrusions.

ORCID

Chang Liu ⓘ http://orcid.org/0000-0001-7257-8563
Lijun Xu ⓘ http://orcid.org/0000-0003-0488-9604

References

1. Lewis, B., and von Elbe, G. (1987) *Combustion, flames and explosions of gases*. 3rd ed. Academic Press, London, UK.
2. Law, C. K. (2006) *Combustion physics*. Cambridge University Press, New York, USA.
3. Moore, R. H., Shook, M., Beyersdorf, A., Corr, C., Herndon, S., Knighton, W. B., Miake-Lye, R., Thornhill, K. L., Winstead, E. L., Yu, Z., Ziemba, L. D., and Anderson, B. E. (2015) Influence of jet fuel composition on aircraft engine emissions: A synthesis of aerosol emissions data from the NASA APEX, AAFEX, and ACCESS Missions. *Energy Fuel* 29(4): 2591–2600. doi:10.1021/ef502618w.
4. Toftegaard, M. B., Brix, J., Jensen, P. A., Glarborg, P., and Jensen, A. D. (2010) Oxy-fuel combustion of solid fuels. *Prog. Energy Combust.* 36(5): 581–625. doi:10.1016/j.pecs.2010.02.001.
5. Dreier, T., Chrystie, R., Endres, T., and Schulz, C. (2006) Laser-based combustion diagnostics. In *Encyclopedia of analytical chemistry*, Meyers, R. A., Ed., John Wiley & Sons, Ltd.
6. Hassel, E. P., and Linow, S. (2000) Laser diagnostics for studies of turbulent combustion. *Meas. Sci. Technol.* 11: R37–R57. doi:10.1088/0957-0233/11/2/201.
7. Hanson, R. K., Spearrin, R. M., and Goldenstein, C. S. (2016) *Spectroscopy and optical diagnostics for gases*. Springer International Publishing, Switzerland.
8. Echbreth, A. C. (1996) *Laser diagnostics for combustion temperature and species*. 2nd ed. Gordon and Breach Science Publishers, Netherlands.
9. Hanson, R. K. (2011) Applications of quantitative laser sensors to kinetics, propulsion and practical energy systems. *Proc. Combust. Inst.* 33(1): 1–40. doi:10.1016/j.proci.2010.09.007.
10. Ehn, A., Zhu, J., Li, X., and Kiefer, J. (2017) Advanced laser-based techniques for gas-phase diagnostics in combustion and aerospace engineering. *Appl. Spectrosc.* 71(3): 341–366. doi:10.1177/0003702817690161.
11. Goldenstein, C. S., Spearrin, R. M., Jeffries, J. B., and Hanson, R. K. (2017) Infrared laser-absorption sensing for combustion gases. *Prog. Energy Combust.* 60: 132–176. doi:10.1016/j.pecs.2016.12.002.
12. Lackner, M. (2007) Tunable diode laser absorption spectroscopy (TDLAS) in the process industries – A review. *Rev. Chem. Eng.* 23(2): 65–147. doi:10.1515/REVCE.2007.23.2.65.
13. Allen, M. G. (1998) Diode laser absorption sensors for gas-dynamic and combustion flows. *Meas. Sci. Technol.* 9(4): 545–562. doi:10.1088/0957-0233/9/4/001.
14. Hendricks, A. G., Vandsburger, U., Saunders, W. R., and Baumann, W. T. (2006) The use of tunable diode laser absorption spectroscopy for the measurement of flame dynamics. *Meas. Sci. Technol.* 17(1): 139–144. doi:10.1088/0957-0233/17/1/023.
15. Schulz, C., and Sick, V. (2005) Tracer-LIF diagnostics: quantitative measurement of fuel concentration, temperature and fuel/air ratio in practical combustion systems. *Prog. Energy Combust.* 31(1): 75–121. doi:10.1016/j.pecs.2004.08.002.
16. Seitzman, J. M., and Hanson, R. K. (1992) Planar fluorescence imaging: Basic concepts for scalar and velocity measurements. In *Combustings flow diagnostics*, Durão, D. F. G., Heitor, M. V., Whitelaw, J. H., Witze, P. O., Eds., Springer Netherlands, Dordrecht, pp. 137–157.
17. Rakovský, J., ermák, P., Musset, O., and Veis, P. (2014) A review of the development of portable laser induced breakdown spectroscopy and its applications. *Spectrochim. Acta B* 101: 269–287. doi:10.1016/j.sab.2014.09.015.
18. Song, K., Lee, Y.-I., and Sneddon, J. (1997) Applications of laser-induced breakdown spectrometry. *Appl. Spectrosc. Rev.* 32(3): 183–235. doi:10.1080/05704929708003314.
19. Sigrist, M. W. (2003) Trace gas monitoring by laser photoacoustic spectroscopy and related techniques (plenary). *Rev. Sci. Instrum.* 74(1): 486–490. doi:10.1063/1.1512697.
20. Elia, A., Lugarà, P. M., Di Franco, C., and Spagnolo, V. (2009) Photoacoustic techniques for trace gas sensing based on semiconductor laser sources. *Sensors* 9(12): 9616–9628. doi:10.3390/s91209616.
21. Kiefer, J., and Ewart, P. (2011) Laser diagnostics and minor species detection in combustion using resonant four-wave mixing. *Prog. Energy Combust.* 37(5): 525–564. doi:10.1016/j.pecs.2010.11.001.

22. Hall, R. J., and Eckbreth, A. C. (1981) Combustion diagnosis by coherent anti-Stokes Raman spectroscopy (CARS). *Opt. Eng.* 20(4): 494–500. doi:10.1117/12.7972754.

23. Roy, S., Gord, J. R., and Patnaik, A. K. (2010) Recent advances in coherent anti-Stokes Raman scattering spectroscopy: Fundamental developments and applications in reacting flows. *Prog. Energy Combust.* 36(2): 280–306. doi:10.1016/j.pecs.2009.11.001.

24. Cai, W., and Kaminski, C. F. (2017) Tomographic absorption spectroscopy for the study of gas dynamics and reactive flows. *Prog. Energy Combust.* 59: 1–31. doi:10.1016/j.pecs.2016.11.002.

25. Slabaugh, C., Pratt, A., and Lucht, R. (2015) Simultaneous 5 kHz OH-PLIF/PIV for the study of turbulent combustion at engine conditions. *Appl. Phys. B-Lasers O* 118(1): 109–130. doi:10.1007/s00340-014-5960-5.

26. Nygren, J., Hult, J., Richter, M., Aldén, M., Christensen, M., Hultqvist, A., and Johansson, B. (2002) Three-dimensional laser induced fluorescence of fuel distributions in an HCCI engine. *Proc. Combust. Inst.* 29(1): 679–685. doi:10.1016/S1540-7489(02)80087-6.

27. Kiefer, J., Tröger, J. W., Li, Z., Seeger, T., Alden, M., and Leipertz, A. (2012) Laser-induced breakdown flame thermometry. *Combust. Flame* 159(12): 3576–3582. doi:10.1016/j.combustflame.2012.08.005.

28. Wynn, C. M., Palmacci, S., Clark, M. L., and Kunz, R. R. (2012) Dynamic photoacoustic spectroscopy for trace gas detection. *Appl. Phys. Lett.* 101(18): 184103. doi:10.1063/1.4764515.

29. Bohlin, A., and Kliewer, C. J. (2013) Communication: Two-dimensional gas-phase coherent anti-Stokes Raman spectroscopy (2D-CARS): Simultaneous planar imaging and multiplex spectroscopy in a single laser shot. *J. Chem. Phys.* 138(22): 221101. doi:10.1063/1.4810876.

30. Wright, P., Terzija, N., Davidson, J. L., Garcia-Castillo, S., Garcia-Stewart, C., Pegrum, S., Colbourne, S., Turner, P., Crossley, S. D., Litt, T., Murray, S., Ozanyan, K. B., and McCann, H. (2010) High-speed chemical species tomography in a multi-cylinder automotive engine. *Chem. Eng. J.* 158(1): 2–10. doi:10.1016/j.cej.2008.10.026.

31. Tsekenis, S. A., Wilson, D., Lengden, M., Hyvönen, J., Leinonen, J., Shah, A., Andersson, Ö., and McCann, H. (2017) Towards in-cylinder chemical species tomography on large-bore IC engines with pre-chamber. *Flow Meas. Instrum.* 53: 116–125. doi:10.1016/j.flowmeasinst.2016.04.006.

32. Rothman, L. S., Gordon, I. E., Babikov, Y., Barbe, A., Chris Benner, D., Bernath, P. F., Birk, M., Bizzocchi, L., Boudon, V., Brown, L. R., Campargue, A., Chance, K., Cohen, E. A., Coudert, L. H., Devi, V. M., Drouin, B. J., Fayt, A., Flaud, J. M., Gamache, R. R., Harrison, J. J., Hartmann, J. M., Hill, C., Hodges, J. T., Jacquemart, D., Jolly, A., Lamouroux, J., Le Roy, R. J., Li, G., Long, D. A., Lyulin, O. M., Mackie, C. J., Massie, S. T., Mikhailenko, S., Müller, H. S. P., Naumenko, O. V., Nikitin, A. V., Orphal, J., Perevalov, V., Perrin, A., Polovtseva, E. R., Richard, C., Smith, M. A. H., Starikova, E., Sung, K., Tashkun, S., Tennyson, J., Toon, G. C., Tyuterev, V. G., and Wagner, G. (2013) The HITRAN2012 molecular spectroscopic database. *J. Quant. Spectrosc. Radiat. Transf.* 130: 4–50. doi:10.1016/j.jqsrt.2013.07.002.

33. Rothman, L. S., Gordon, I. E., Barber, R. J., Dothe, H., Gamache, R. R., Goldman, A., Perevalov, V. I., Tashkun, S. A., and Tennyson, J. (2010) HITEMP, the High-Temperature Molecular Spectroscopic Database. *J. Quant. Spectrosc. Radiat. Transf.* 111: 2139–2150. doi:10.1016/j.jqsrt.2010.05.001.

34. Hinkley, E. D. (1976) Laser spectroscopic instrumentation and techniques: Long-path monitoring by resonance absorption. *Opt. Quant. Electron.* 8(2): 155–167. doi:10.1007/BF00619441.

35. Hanson, R. K., Kuntzand, P. A., and Kruger, C. H. (1977) High-resolution spectroscopy of combustion gases using a tunable IR diode laser. *Appl. Opt.* 16: 2045–2047. doi:10.1364/AO.16.002045.

36. Arroyo, M. P., and Hanson, R. K. (1993) Absorption measurements of water-vapor concentration, temperature, and line-shape parameters using a tunable InGaAsP diode laser. *Appl. Opt.* 32 (30): 6104–6116. doi:10.1364/AO.32.006104.

37. Upschulte, B. L., Sonnenfroh, D. M., and Allen, M. G. (1999) Measurements of CO, CO_2, OH, and H_2O in room-temperature and combustion gases by use of a broadly current-tuned multi-section InGaAsP diode laser. *Appl. Opt.* 38(9): 1506–1512. doi:10.1364/AO.38.001506.

38. Hira, N., and Yasir, J. (2013) Recent advancements in spectroscopy using tunable diode lasers. *Laser Phys. Lett.* 10(4): 043001. doi:10.1088/1612-2011/10/4/043001.

39. Razeghi, M., Lu, Q. Y., Bandyopadhyay, N., Zhou, W., Heydari, D., Bai, Y., and Slivken, S. (2015) Quantum cascade lasers: from tool to product. *Opt. Express* 23(7): 8462–8475. doi:10.1364/OE.23.008462.

40. Zeller, W., Naehle, L., Fuchs, P., Gerschuetz, F., Hildebrandt, L., and Koeth, J. (2010) DFB lasers between 760 nm and 16 μm for sensing applications. *Sensors (Basel, Switzerland)* 10(4): 2492–2510. doi:10.3390/s100402492.

41. Michalzik, R. (2013) VCSELs: A research review. In *VCSELs: Fundamentals, technology and applications of vertical-cavity surface-emitting lasers*, Michalzik, R., Ed., Springer, Berlin, Heidelberg, pp. 3–18.

42. Huber, R., Wojtkowski, M., and Fujimoto, J. G. (2006) Fourier domain mode locking (FDML): A new laser operating regime and applications for optical coherence tomography. *Opt. Express* 14(8): 3225–3237. doi:10.1364/OE.14.003225.

43. Kranendonk, L. A., An, X., Caswell, A. W., Herold, R. E., Sanders, S. T., Huber, R., Fujimoto, J. G., Okura, Y., and Urata, Y. (2007) High speed engine gas thermometry by Fourier-domain mode-locked laser absorption spectroscopy. *Opt. Express* 15(23): 15115–15128. doi:10.1364/OE.15.015115.

44. Tittel, F. K., Bakhirkin, Y., Kosterev, A. A., and Wysocki, G. (2006) Recent advances in trace gas detection using quantum and interband cascade lasers. *Rev. Laser Eng.* 34(4): 275–282. doi:10.2184/lsj.34.275.

45. Vurgaftman, I., Weih, R., Kamp, M., Meyer, J. R., Canedy, C. L., Kim, C. S., Kim, M., Bewley, W. W., Merritt, C. D., Abell, J., and Höfling, S. (2015) Interband cascade lasers. *J. Phys. D: Appl. Phys.* 48(12): 123001. doi:10.1088/0022-3727/48/12/123001.

46. Vitiello, M. S., Scalari, G., Williams, B., and De Natale, P. (2015) Quantum cascade lasers: 20 years of challenges. *Opt. Express* 23(4): 5167–5182. doi:10.1364/OE.23.005167.

47. Li, J. S., Chen, W., and Fischer, H. (2013) Quantum cascade laser spectrometry techniques: A new trend in atmospheric chemistry. *Appl. Spectrosc. Rev.* 48(7): 523–559. doi:10.1080/05704928.2012.757232.

48. Werblinski, T., Engel, S. R., Engelbrecht, R., Zigan, L., and Will, S. (2013) Temperature and multi-species measurements by supercontinuum absorption spectroscopy for IC engine applications. *Opt. Express* 21(11): 13656–13667. doi:10.1364/OE.21.013656.

49. Witzel, O., Klein, A., Meffert, C., Wagner, S., Kaiser, S., Schulz, C., and Ebert, V. (2013) VCSEL-based, high-speed, in situ TDLAS for incylinder water vapor measurements in IC engines. *Opt. Express* 21(17): 19951–19965. doi:10.1364/OE.21.019951.

50. Goldenstein, C. S., Almodóvar, C. A., Jeffries, J. B., Hanson, R. K., and Brophy, C. M. (2014) High-bandwidth scanned-wavelength-modulation spectroscopy sensors for temperature and H_2O in a rotating detonation engine. *Meas. Sci. Technol.* 25: 105104. doi:10.1088/0957-0233/25/10/105104.

51. Sanders, S. T., Baldwin, J. A., Jenkins, T. P., Baer, D. S., and Hanson, R. K. (2000) Diode-laser sensor for monitoring multiple combustion parameters in pulse detonation engines. *Proc. Combust. Inst.* 28(1): 587–594. doi:10.1016/S0082-0784(00)80258-1.

52. Li, H., Farooq, A., Jeffries, J. B., and Hanson, R. K. (2007) Near-infrared diode laser absorption sensor for rapid measurements of temperature and water vapor in a shock tube. *Appl. Phys. B-Lasers O* 89: 407–416. doi:10.1007/s00340-007-2781-9.

53. Hanson, R. K., and Davidson, D. F. (2014) Recent advances in laser absorption and shock tube methods for studies of combustion chemistry. *Prog. Energy Combust.* 44: 103–114. doi:10.1016/j.pecs.2014.05.001.

54. Schultz, I. A., Goldenstein, C. S., Strand, C. L., Jeffries, J. B., Hanson, R. K., and Goyne, C. P. (2014) Hypersonic scramjet testing via diode laser absorption in a reflected shock tunnel. *J. Propuls. Power* 30(6): 1586–1594. doi:10.2514/1.B35220.

55. Sur, R., Wang, S., Sun, K., Davidson, D. F., Jeffries, J. B., and Hanson, R. K. (2015) High-sensitivity interference-free diagnostic for measurement of methane in shock tubes. *J. Quant. Spectrosc. Radiat. Transf.* 156: 80–87. doi:10.1016/j.jqsrt.2015.01.023.

56. Teichert, H., Fernholz, T., and Ebert, V. (2003) Simultaneous in situ measurement of CO, H_2O, and gas temperatures in a full-sized coal-fired power plant by near-infrared diode lasers. *Appl. Opt.* 42(12): 2043–2051. doi:10.1364/AO.42.002043.

57. Chao, X., Jeffries, J., and Hanson, R. (2013) Real-time, in situ, continuous monitoring of CO in a pulverized-coal-fired power plant with a 2.3 μm laser absorption sensor. *Appl. Phys. B-Lasers O* 110(3): 359–365. doi:10.1007/s00340-012-5262-8.

58. Deguchi, Y., Kamimoto, T., Wang, Z. Z., Yan, J. J., Liu, J. P., Watanabe, H., and Kurose, R. (2014) Applications of laser diagnostics to thermal power plants and engines. *Appl. Therm. Eng.* 73(2): 1453–1464. doi:10.1016/j.applthermaleng.2014.05.063.

59. Reid, J., and Labrie, D. (1981) Second-harmonic detection with tunable diode lasers – Comparison of experiment and theory. *Appl. Phys. B-Lasers O* 26(3): 203–210. doi:10.1007/BF00692448.

60. York, T., McCann, H., and Ozanyan, K. B. (2011) Agile sensing systems for tomography. *IEEE Sens. J.* 11(12): 3086–3105. doi:10.1109/JSEN.2011.2164905.

61. McCann, H., Wright, P., and Daun, K. (2015) Chemical species tomography. In *Industrial tomography: Systems and applications*, Wang, M., Ed., Woodhead Publishing, Cambridge, UK, pp. 135–174.

62. Martin, P. A. (2002) Near-infrared diode laser spectroscopy in chemical process and environmental air monitoring. *Chem. Soc. Rev.* 31: 201–210. doi:10.1039/b003936p.

63. Bolshov, M. A., Kuritsyn, Y. A., and Romanovskii, Y. V. (2015) Tunable diode laser spectroscopy as a technique for combustion diagnostics. *Spectrochim. Acta B* 106: 45–66. doi:10.1016/j.sab.2015.01.010.

64. Klingbeil, A. E., Jeffries, J. B., and Hanson, R. K. (2007) Design of a fiber-coupled mid-infrared fuel sensor for pulse detonation engines. *AIAA J.* 45(4): 772–778. doi:10.2514/1.26504.

65. Spearrin, R. M., Li, S., Davidson, D. F., Jeffries, J. B., and Hanson, R. K. (2015) High-temperature iso-butene absorption diagnostic for shock tube kinetics using a pulsed quantum cascade laser near 11.3 μm. *Proc. Combust. Inst.* 35(3): 3645–3651. doi:10.1016/j.proci.2014.04.002.

66. D. S. Baer, V. N. (1996) Scanned- and fixed-wavelength absorption diagnostics for combustion measurements using multiplexed diode lasers. *AIAA J.* 34(3): 489–493. doi:10.2514/3.13094.

67. Yang, H., Guo, X., Zhou, W., Chen, B., Hu, J., Su, M., and Cai, X. (2015) Investigation on liquid film of urea water solutions with diode laser absorption spectroscopy. *Exp. Fluids* 56(4): 73. doi:10.1007/s00348-015-1941-7.

68. Kamimoto, T., Deguchi, Y., Shisawa, Y., Kitauchi, Y., and Eto, Y. (2016) Development of fuel composition measurement technology using laser diagnostics. *Appl. Therm. Eng.* 102: 596–603. doi:10.1016/j.applthermaleng.2016.03.075.

69. Stacewicz, T., Bielecki, Z., Wojtas, J., Magryta, P., Mikolajczyk, J., and Szabra, D. (2016) Detection of disease markers in human breath with laser absorption spectroscopy. *Opto-Electron. Rev.* 24(2): 82–94. doi:10.1515/oere-2016-0011.

70. Jatana, G., Geckler, S., Koeberlein, D., and Partridge, W. (2017) Design and development of a probe-based multiplexed multi-species absorption spectroscopy sensor for characterizing transient gas-parameter distributions in the intake systems of I.C. engines. *Sens. Actuators B-Chem.* 240: 1197–1204. doi:10.1016/j.snb.2016.08.183.

71. Zhou, X. (2005) *Diode-laser absorption sensors for combustion control*, Ph.D. dissertation, Stanford University, Department of Mechanical Engineering.

72. Zhou, X., Liu, X., Jeffries, J. B., and Hanson, R. K. (2005) Selection of NIR H_2O absorption transitions for in-cylinder measurement of temperature in IC engines. *Meas. Sci. Technol.* 16(12): 2437–2445. doi:10.1088/0957-0233/16/12/006.

73. Zhou, X., Liu, X., Jeffries, J. B., and Hanson, R. K. (2003) Development of a sensor for temperature and water concentration in combustion gases using a single tunable diode laser. *Meas. Sci. Technol.* 14(8): 1459–1468. doi:10.1088/0957-0233/14/8/335.

74. Liu, X., Jeffries, J. B., Hanson, R. K., Hinckley, K. M., and Woodmansee, M. A. (2006) Development of a tunable diode laser sensor for measurements of gas turbine exhaust temperature. *Appl. Phys. B-Lasers O* 82: 469–478. doi:10.1007/s00340-005-2078-9.

75. Li, S., Farooq, A., and Hanson, R. K. (2011) H_2O temperature sensor for low-pressure flames using tunable diode laser absorption near 2.9 μm. *Meas. Sci. Technol.* 22(12): 125301. doi:10.1088/0957-0233/22/12/125301.

76. Ouyang, X., and Varghese, P. L. (1990) Selection of spectral lines for combustion diagnostics. *Appl. Opt.* 29(33): 4884–4890. doi:10.1364/AO.29.004884.

77. Li, F., Yu, X., Gu, H., Li, Z., Zhao, Y., Ma, L., Chen, L., and Chang, X. (2011) Simultaneous measurements of multiple flow parameters for scramjet characterization using tunable diode-laser sensors. *Appl. Opt.* 50(36): 6697–6707. doi:10.1364/AO.50.006697.

78. Klein, A., Witzel, O., and Ebert, V. (2014) Rapid, time-division multiplexed, direct absorption- and wavelength modulation-spectroscopy. *Sensors* 14: 21497–21513. doi:10.3390/s141121497.

79. Liu, J. T. C., Rieker, G. B., Jeffries, J. B., Gruber, M. R., Carter, C. D., Mathur, T., and Hanson, R. K. (2005) Near-infrared diode laser absorption diagnostic for temperature and water vapor in a scramjet combustor. *Appl. Opt.* 44(31): 6701–6711. doi:10.1364/AO.44.006701.

80. Pan, R., Jeffries, J. B., Dreier, T., and Schulz, C. (2015) Measurements of liquid film thickness, concentration and temperature of aqueous NaCl solution by NIR absorption spectroscopy. *Appl. Phys. B-Lasers O* 120(3): 397–406. doi:10.1007/s00340-015-6149-2.

81. Sanders, S. T., Mattison, D. W., Ma, L., Jeffries, J. B., and Hanson, R. K. (2002) Wavelength-agile diode-laser sensing strategies for monitoring gas properties in optically harsh flows: Application in cesium-seeded pulse detonation engine. *Opt. Express* 10(12): 505–514. doi:10.1364/OE.10.000505.

82. Göran Blume, N., and Wagner, S. (2015) Broadband supercontinuum laser absorption spectrometer for multiparameter gas phase combustion diagnostics. *Opt. Lett.* 40(13): 3141–3144. doi:10.1364/OL.40.003141.

83. Dulov, E. N., and Khripunov, D. M. (2007) Voigt lineshape function as a solution of the parabolic partial differential equation. *J. Quant. Spectrosc. Radiat. Transf.* 107(3): 421–428. doi:10.1016/j.jqsrt.2007.03.003.

84. Mendenhall, M. H. (2007) Fast computation of Voigt functions via Fourier transforms. *J. Quant. Spectrosc. Radiat. Transf.* 105(3): 519–524. doi:10.1016/j.jqsrt.2006.11.014.

85. Xu, L., Liu, C., Zheng, D., Cao, Z., and Cai, W. (2014) Digital signal processor-based high-precision on-line Voigt lineshape fitting for direct absorption spectroscopy. *Rev. Sci. Instrum.* 85(12): 123108. doi:10.1063/1.4903356.

86. Werle, P., Mücke, R., and Slemr, F. (1993) The limits of signal averaging in atmospheric trace-gas monitoring by tunable diode-laser absorption spectroscopy (TDLAS). *Appl. Phys. B-Lasers O* 57(2): 131–139. doi:10.1007/BF00425997.

87. Li, J., Yu, B., Zhao, W., and Chen, W. (2014) A review of signal enhancement and noise reduction techniques for tunable diode laser absorption spectroscopy. *Appl. Spectrosc. Rev.* 49(8): 666–691. doi:10.1080/05704928.2014.903376.

88. Schilt, S., Thévenaz, L., and Robert, P. (2003) Wavelength modulation spectroscopy: Combined frequency and intensity laser modulation. *Appl. Opt.* 42(33): 6728–6738. doi:10.1364/AO.42.006728.

89. Rieker, G. B. (2009) *Wavelength-modulation spectroscopy for measurements of gas temperature and concentration in harsh environments.* Ph.D. dissertation, Stanford University, Department of Mechanical Engineering.

90. Huang, Q.-x., Wang, F., Zhang, H.-d., Yan, J.-h., Ni, M.-j., and Cen, K.-f. (2013) In-situ CO measurement of gas and oil combustion flame using near infrared tunable diode laser with direct and modulated absorption signals. *Opt. Commun.* 306: 99–105. doi:10.1016/j.optcom.2013.05.047.

91. Li, H., Rieker, G. B., Liu, X., Jeffries, J. B., and Hanson, R. K. (2006) Extension of wavelength-modulation spectroscopy to large modulation depth for diode laser absorption measurements in high-pressure gases. *Appl. Opt.* 45(5): 1052–1061. doi:10.1364/AO.45.001052.

92. Liu, J. T. C., Jeffries, J. B., and Hanson, R. K. (2004) Wavelength modulation absorption spectroscopy with 2f detection using multiplexed diode lasers for rapid temperature measurements in gaseous flows. *Appl. Phys. B-Lasers O* 78(3–4): 503–511. doi:10.1007/s00340-003-1380-7.

93. Wang, F., Cen, K. F., Li, N., Huang, Q. X., Chao, X., Yan, J. H., and Chi, Y. (2010) Simultaneous measurement on gas concentration and particle mass concentration by tunable diode laser. *Flow Meas. Instrum.* 21(3): 382–387. doi:10.1016/j.flowmeasinst.2010.04.009.

94. Liu, J. T. C., Jeffries, J. B., and Hanson, R. K. (2004) Large-modulation-depth 2f spectroscopy with diode lasers for rapid temperature and species measurements in gases with blended and broadened spectra. *Appl. Opt.* 43(35): 6500–6509. doi:10.1364/AO.43.006500.

95. Philippe, L. C., and Hanson, R. K. (1993) Laser diode wavelength-modulation spectroscopy for simultaneous measurement of temperature, pressure, and velocity in shock-heated oxygen flows. *Appl. Opt.* 32(30): 6090–6103. doi:10.1364/AO.32.006090.

96. Silver, J. A. (1999) Diode laser measurements of concentration and temperature in microgravity combustion. *Meas. Sci. Technol.* 10: 845–852. doi:10.1088/0957-0233/10/10/303.

97. Li, H., Zhou, X., Jeffries, J. B., and Hanson, R. K. (2007) Sensing and control of combustion instabilities in swirl-stabilized combustors using diode-laser absorption. *AIAA J.* 45(2): 390–398. doi:10.2514/1.24774.

98. Rieker, G. B., Jeffries, J. B., and Hanson, R. K. (2009) Calibration-free wavelength-modulation spectroscopy for measurements of gas temperature and concentration in harsh environments. *Appl. Opt.* 48(29): 5546–5560. doi:10.1364/AO.48.005546.

99. Chao, X., Jeffries, J. B., and Hanson, R. K. (2009) Absorption sensor for CO in combustion gases using 2.3 μm tunable diode lasers. *Meas. Sci. Technol.* 20(11): 115201 (9pp). doi:10.1088/0957-0233/20/11/115201.

100. Peng, Z., Ding, Y., Che, L., Li, X., and Zheng, K. (2011) Calibration-free wavelength modulated TDLAS under high absorbance conditions. *Opt. Express* 19(23): 23104–23110. doi:10.1364/OE.19.023104.

101. Lan, L. J., Ding, Y. J., Peng, Z. M., Du, Y. J., and Liu, Y. F. (2014) Calibration-free wavelength modulation for gas sensing in tunable diode laser absorption spectroscopy. *Appl. Phys. B-Lasers O* 117(4): 1211–1219. doi:10.1007/s00340-014-5945-4.

102. Rieker, G. B., Li, H., Liu, X., Jeffries, J. B., Hanson, R. K., Allen, M. G., Wehe, S. D., Mulhall, P. A., and Kindle, H. S. (2007) A diode laser sensor for rapid, sensitive measurements of gas temperature and water vapour concentration at high temperatures and pressures. *Meas. Sci. Technol.* 18 (5): 1195–1204. doi:10.1088/0957-0233/18/5/005.

103. Spearrin, R. M., Goldenstein, C. S., Jeffries, J. B., and Hanson, R. K. (2013) Fiber-coupled 2.7 μm laser absorption sensor for CO_2 in harsh combustion environments. *Meas. Sci. Technol.* 24: 055107 (11pp). doi:10.1088/0957-0233/24/5/055107.

104. Kluczynski, P., and Axner, O. (1999) Theoretical description based on Fourier analysis of wavelength-modulation spectrometry in terms of analytical and background signals. *Appl. Opt.* 38 (27): 5803–5815. doi:10.1364/AO.38.005803.

105. Schultz, I. A., Goldenstein, C. S., Jeffries, J. B., Hanson, R. K., Rockwell, R. D., and Goyne, C. P. (2014) Diode laser absorption sensor for combustion progress in a model scramjet. *J. Propuls. Power* 30(3): 550–557. doi:10.2514/1.B34905.

106. Sun, K., Chao, X., Sur, R., Goldenstein, C. S., Jeffries, J. B., and Hanson, R. K. (2013) Analysis of calibration-free wavelength-scanned wavelength modulation spectroscopy for practical gas sensing using tunable diode lasers. *Meas. Sci. Technol.* 24(12): 125203. doi:10.1088/0957-0233/24/12/125203.

107. Goldenstein, C. S., Strand, C. L., Schultz, I. A., Sun, K., Jeffries, J. B., and Hanson, R. K. (2014) Fitting of calibration-free scanned-wavelength-modulation spectroscopy spectra for determination of gas properties and absorption lineshapes. *Appl. Opt.* 53(3): 356–367. doi:10.1364/AO.53.000356.

108. Qu, Z., Ghorbani, R., Valiev, D., and Schmidt, F. M. (2015) Calibration-free scanned wavelength modulation spectroscopy-application to H_2O and temperature sensing in flames. *Opt. Express* 23 (12): 16492–16499. doi:10.1364/OE.23.016492.

109. Goldenstein, C. S., Spearrin, R. M., Schultz, I. A., Jeffries, J. B., and Hanson, R. K. (2014) Wavelength-modulation spectroscopy near 1.4 μm for measurements of H_2O and temperature in high-pressure and temperature gases. *Meas. Sci. Technol.* 25: 055101. doi:10.1088/0957-0233/25/5/055101.

110. Goldenstein, C. S., Schultz, I. A., Spearrin, R. M., Jeffries, J. B., and Hanson, R. K. (2014) Scanned-wavelength-modulation spectroscopy near 2.5 μm for H_2O and temperature in a hydrocarbon-fueled scramjet combustor. *Appl. Phys. B-Lasers O* 116(3): 717–727. doi:10.1007/s00340-013-5755-0.

111. Spearrin, R. M., Goldenstein, C. S., Schultz, I. A., Jeffries, J. B., and Hanson, R. K. (2014) Simultaneous sensing of temperature, CO, and CO_2 in a scramjet combustor using quantum cascade laser absorption spectroscopy. *Appl. Phys. B-Lasers O* 117(2): 689–698. doi:10.1007/s00340-014-5884-0.

112. Sun, K., Sur, R., Jeffries, J., Hanson, R., Clark, T., Anthony, J., Machovec, S., and Northington, J. (2014) Application of wavelength-scanned wavelength-modulation spectroscopy H_2O absorption measurements in an engineering-scale high-pressure coal gasifier. *Appl. Phys. B-Lasers O* 117(1): 411–421. doi:10.1007/s00340-014-5850-x.

113. Sur, R., Sun, K., Jeffries, J., Hanson, R., Pummill, R., Waind, T., Wagner, D., and Whitty, K. (2014) TDLAS-based sensors for in situ measurement of syngas composition in a pressurized, oxygen-blown, entrained flow coal gasifier. *Appl. Phys. B-Lasers O* 116(1): 33–42. doi:10.1007/s00340-013-5644-6.

114. Sur, R., Sun, K., Jeffries, J. B., Socha, J. G., and Hanson, R. K. (2015) Scanned-wavelength-modulation-spectroscopy sensor for CO, CO_2, CH_4 and H_2O in a high-pressure engineering-scale transport-reactor coal gasifier. *Fuel* 150: 102–111. doi:10.1016/j.fuel.2015.02.003.

115. Ouyang, X., and Varghese, P. L. (1989) Line-of-sight absorption measurements of high temperature gases with thermal and concentration boundary layers. *Appl. Opt.* 28: 3979–3984. doi:10.1364/AO.28.003979.

116. Wang, J., Maiorov, M., Jeffries, J. B., Garbuzov, D. Z., Connolly, J. C., and Hanson, R. K. (2000) A potential remote sensor of CO in vehicle exhausts using 2.3 micron diode lasers. *Meas. Sci. Technol.* 11(11): 1576–1584. doi:10.1088/0957-0233/11/11/306.

117. Smith, C. H., Goldenstein, C. S., and Hanson, R. K. (2014) A scanned-wavelength-modulation absorption-spectroscopy sensor for temperature and H_2O in low-pressure flames. *Meas. Sci. Technol.* 25: 115501 (13pp). doi:10.1088/0957-0233/25/11/115501.

118. Goldenstein, C. S., Schultz, I. A., Jeffries, J. B., and Hanson, R. K. (2013) Two-color absorption spectroscopy strategy for measuring the column density and path average temperature of the absorbing species in nonuniform gases. *Appl. Opt.* 52(33): 7950–7962. doi:10.1364/AO.52.007950.

119. Sanders, S. T., Wang, J., Jeffries, J. B., and Hanson, R. K. (2001) Diode-laser absorption sensor for line-of-sight gas temperature distributions. *Appl. Opt.* 40(24): 4404–4415. doi:10.1364/AO.40.004404.

120. Liu, X., Jeffries, J. B., and Hanson, R. K. (2007) Measurement of nonuniform temperature distributions using line-of-sight absorption spectroscopy. *AIAA J.* 45(2): 411–419. doi:10.2514/1.26708.

121. Ma, L. H., Lau, L. Y., and Ren, W. (2017) Non-uniform temperature and species concentration measurements in a laminar flame using multi-band infrared absorption spectroscopy. *Appl. Phys. B-Lasers O* 123(3): 83. doi:10.1007/s00340-017-6645-7.

122. Liu, C., Xu, L., and Cao, Z. (2013) Measurement of nonuniform temperature and concentration distributions by combining line-of-sight TDLAS with regularization methods. *Appl. Opt.* 52(20): 4827–4842. doi:10.1364/AO.52.004827.

123. Prucker, S., Meier, W., and Stricker, W. (1994) A flat flame burner as calibration source for combustion research: Temperatures and species concentrations of premixed H_2/air flames. *Rev. Sci. Instrum.* 65(9): 2908–2911. doi:10.1063/1.1144637.

124. Simmons, F. S. (2000) *Rocket exhaust plume phenomenology*. The Aerospace Press, El Segundo, California.

125. Dasch, C. J. (1992) One-dimensional tomography: A comparison of Abel, onion-peeling, and filtered backprojection methods. *Appl. Opt.* 31(8): 1146–1152. doi:10.1364/AO.31.001146.

126. Villarreal, R., and Varghese, P. (2005) Frequency-resolved absorption tomography with tunable diode lasers. *Appl. Opt.* 44(31): 6786–6795. doi:10.1364/AO.44.006786.

127. Daun, K. J., Thomson, K. A., Liu, F., and Smallwood, G. J. (2006) Deconvolution of axisymmetric flame properties using Tikhonov regularization. *Appl. Opt.* 45(19): 4638–4646. doi:10.1364/AO.45.004638.

128. Guha, A., and Schoegl, I. (2014) Tomographic laser absorption spectroscopy using Tikhonov regularization. *Appl. Opt.* 53(34): 8095–8103. doi:10.1364/AO.53.008095.

129. Liu, C., Xu, L., Li, F., Cao, Z., Tsekenis, S., and McCann, H. (2015) Resolution-doubled one-dimensional wavelength modulation spectroscopy tomography for flame flatness validation of a flat-flame burner. *Appl. Phys. B-Lasers O* 120(3): 407–416. doi:10.1007/s00340-015-6150-9.

130. Liu, C., Xu, L., Cao, Z., and McCann, H. (2014) Reconstruction of axisymmetric temperature and gas concentration distributions by combining fan-beam TDLAS with onion-peeling deconvolution. *IEEE T. Instrum. Meas.* 63(12): 3067–3075. doi:10.1109/TIM.2014.2315737.

131. Hsich, J. (2009) *Computed tomography principles, design, artifacts, and recent advances*. SPIE Press, Bellingham, Washington, USA.

132. Liu, C., Cao, Z., Li, F., Lin, Y., and Xu, L. (2017) Flame monitoring of a model swirl injector using 1D tunable diode laser absorption spectroscopy tomography. *Meas. Sci. Technol.* 28(5): 054002. doi:10.1088/1361-6501/aa5aee.

133. Gorenflo, R., and Vessella, S. (1993) *Abel integral equations: Analysis and applications*. Springer-Verlag, Berlin, Heidelberg.

134. Kesson, E. O. A. A., and Daun, K. J. (2008) Parameter selection methods for axisymmetric flame tomography through Tikhonov regularization. *Appl. Opt.* 47(3): 407–416. doi:10.1364/AO.47.000407.

135. Ginat, D. T., and Gupta, R. (2014) Advances in computed tomography imaging technology. *Annu. Rev. Biomed. Eng.* 16(1): 431–453. doi:10.1146/annurev-bioeng-121813-113601.

136. Tsekenis, S. A., Tait, N., and McCann, H. (2015) Spatially resolved and observer-free experimental quantification of spatial resolution in tomographic images. *Rev. Sci. Instrum.* 86(3): 035104. doi:10.1063/1.4913922.

137. Daun, K. J., Grauer, S. J., and Hadwin, P. J. (2016) Chemical species tomography of turbulent flows: Discrete ill-posed and rank deficient problems and the use of prior information. *J. Quant. Spectrosc. Radiat. Transf.* 172: 58–74. doi:10.1016/j.jqsrt.2015.09.011.

138. Pan, X., Sidky, E. Y., and Vannier, M. (2009) Why do commercial CT scanners still employ traditional, filtered back-projection for image reconstruction? *Inverse Probl.* 25(12): 123009. doi:10.1088/0266-5611/25/12/123009.

139. Beiting, E. J. (1992) Fiber-optic fan-beam absorption tomography. *Appl. Opt.* 31(9): 1328–1343. doi:10.1364/AO.31.001328.

140. Beister, M., Kolditz, D., and Kalender, W. A. (2012) Iterative reconstruction methods in X-ray CT. *Phys. Medica* 28: 94–108. doi:10.1016/j.ejmp.2012.01.003.

141. Kak, A. C., and Slaney, M. (2001) *Principles of computerized tomographic imaging*. Society for Industrial and Applied Mathematics, Philadelphia, USA.

142. Gordon, R., Bender, R., and Herman, G. T. (1970) Algebraic Reconstruction Techniques (ART) for three-dimensional electron microscopy and X-ray photography. *J. Theor. Biol.* 29(3): 471–481. doi:10.1016/0022-5193(70)90109-8.

143. Hansen, P. C., and Saxild-Hansen, M. (2012) AIR Tools-A MATLAB package of algebraic iterative reconstruction methods. *J. Comput. Appl. Math.* 236(8): 2167–2178. doi:10.1016/j.cam.2011.09.039.

144. Hindle, F. P., Carey, S. J., Ozanyan, K., Winterbone, D. E., Clough, E., and McCann, H. (2001) Measurement of gaseous hydrocarbon distribution by a near-infrared absorption tomography system. *J. Electron. Imaging* 10(3): 593–600. doi:10.1117/1.1377306.

145. Gordon, R. (1974) A tutorial on ART (algebraic reconstruction techniques). *IEEE Trans. Nucl. Sci.* 21(3): 78–93. doi:10.1109/TNS.1974.6499238.

146. Andersen, A. H., and Kak, A. C. (1984) Simultaneous algebraic reconstruction technique (SART): A superior implementation of the ART algorithm. *Ultrason. Imaging* 6(1): 81–94. doi:10.1177/016173468400600107.

147. Drescher, A. C., Gadgil, A. J., Price, P. N., and Nazaroff, W. W. (1996) Novel approach for tomographic reconstruction of gas concentration distributions in air: Use of smooth basis functions and simulated annealing. *Atmos. Environ.* 30(6): 929–940. doi:10.1016/1352-2310 (95)00295-2.

148. Fischer, M. L., Price, P. N., Thatcher, T. L., Schwalbe, C. A., Craig, M. J., Wood, E. E., Sextro, R. G., and Gadgil, A. J. (2001) Rapid measurements and mapping of tracer gas concentrations in a large indoor space. *Atmos. Environ.* 35(16): 2837–2844. doi:10.1016/S1352-2310(01)00081-4.

149. Wang, F., Cen, K. F., Li, N., Jeffries, J. B., Huang, Q. X., Yan, J. H., and Chi, Y. (2010) Two-dimensional tomography for gas concentration and temperature distributions based on tunable diode laser absorption spectroscopy. *Meas. Sci. Technol.* 21(4): 045301(10pp). doi:10.1088/0957-0233/21/4/045301.

150. Kasyutich, V., and Martin, P. (2011) Towards a two-dimensional concentration and temperature laser absorption tomography sensor system. *Appl. Phys. B-Lasers O* 102(1): 149–162. doi:10.1007/s00340-010-4123-6.

151. Song, J., Hong, Y., Wang, G., and Pan, H. (2013) Algebraic tomographic reconstruction of two-dimensional gas temperature based on tunable diode laser absorption spectroscopy. *Appl. Phys. B-Lasers O* 112(4): 529–537. doi:10.1007/s00340-013-5435-0.

152. Wang, F., Wu, Q., Huang, Q., Zhang, H., Yan, J., and Cen, K. (2015) Simultaneous measurement of 2-dimensional H_2O concentration and temperature distribution in premixed methane/air flame using TDLAS-based tomography technology. *Opt. Commun.* 346: 53–63. doi:10.1016/j.optcom.2015.02.015.

153. Xia, H., Kan, R., Xu, Z., He, Y., Liu, J., Chen, B., Yang, C., Yao, L., Wei, M., and Zhang, G. (2017) Two-step tomographic reconstructions of temperature and species concentration in a flame based on laser absorption measurements with a rotation platform. *Opt. Laser Eng.* 90: 10–18. doi:10.1016/j.optlaseng.2016.09.005.

154. Engl, H. W., Hanke, M., and Neubauer, A. (2000) *Regularization of inverse problems*. Kluwer Academic Publishers, Dordrecht, Netherlands.

155. Tikhonov, A. N., and Arsenin, V. Y. (1977) *Solutions of ill-posed problems*. Winston & Sons, Washington, DC.

156. Grauer, S. J., Hadwin, P. J., and Daun, K. J. (2016) Bayesian approach to the design of chemical species tomography experiments. *Appl. Opt.* 55(21): 5772–5782. doi:10.1364/AO.55.005772.

157. Grauer, S. J., Hadwin, P. J., and Daun, K. J. (2017) Improving chemical species tomography of turbulent flows using covariance estimation. *Appl. Opt.* 56(13): 3900–3912. doi:10.1364/AO.56.003900.

158. Daun, K. J. (2010) Infrared species limited data tomography through Tikhonov reconstruction. *J. Quant. Spectrosc. Radiat. Transf.* 111(1): 105–115. doi:10.1016/j.jqsrt.2009.08.003.

159. Hansen, P. C., and O'Leary, D. P. (1993) The use of the L-curve in the regularization of discrete ill-posed problems. *SIAM J. Sci. Comput.* 14: 1487–1503. doi:10.1137/0914086.

160. Yang, W. Q., Spink, D. M., York, T. A., and McCann, H. (1999) An image-reconstruction algorithm based on Landweber's iteration method for electrical-capacitance tomography. *Meas. Sci. Technol.* 10(11): 1065–1069. doi:10.1088/0957-0233/10/11/315.

161. Wright, P., Garcia-Stewart, C., Carey, S., Hindle, F., Pegrum, S., Colbourne, S., Turner, P., Hurr, W., Litt, T., Murray, S., Crossley, S., Ozanyan, K., and McCann, H. (2005) Toward in-cylinder absorption tomography in a production engine. *Appl. Opt.* 44(31): 6578–6592. doi:10.1364/AO.44.006578.

162. Terzija, N., Davidson, J. L., Garcia-Stewart, C. A., Wright, P., Ozanyan, K. B., Pegrum, S., Litt, T. J., and McCann, H. (2008) Image optimization for chemical species tomography with an irregular and sparse beam array. *Meas. Sci. Technol.* 19(9): 094007. doi:10.1088/0957-0233/19/9/094007.

163. Wood, M. P., and Ozanyan, K. B. (2013) Concentration and temperature tomography at elevated pressures. *IEEE Sens. J.* 13(8): 3060–3066. doi:10.1109/JSEN.2013.2260535.

164. Liu, C., Xu, L., Chen, J., Cao, Z., Lin, Y., and Cai, W. (2015) Development of a fan-beam TDLAS-based tomographic sensor for rapid imaging of temperature and gas concentration. *Opt. Express* 23(17): 22494–22511. doi:10.1364/OE.23.022494.

165. Wood, M. P., and Ozanyan, K. B. (2015) Simultaneous temperature, concentration, and pressure imaging of water vapor in a turbine engine. *IEEE Sens. J.* 15(1): 545–551. doi:10.1109/JSEN.2014.2349796.

166. Xu, L., Liu, C., Jing, W., Cao, Z., Xue, X., and Lin, Y. (2016) Tunable diode laser absorption spectroscopy-based tomography system for on-line monitoring of two-dimensional distributions of temperature and H_2O mole fraction. *Rev. Sci. Instrum.* 87(1): 013101. doi:10.1063/1.4939052.

167. Wright, P., McCormick, D., Kliment, J., Ozanyan, K., Johnson, M., Black, J., Tsekenis, S. A., Fisher, E., McCann, H., Lengden, M., Wilson, D., Johnstone, W., Archilla, V., González-Núñez, A., Feng, Y., and Nilsson, J. (2016) *Implementation of non-intrusive jet exhaust species distribution measurements within a test facility*. In Paper presented at the 2016 IEEE Aerospace Conference, pp. 1–14.

168. Beiting, E. J. (1991) Fast optical absorption tomography. *Opt. Lett.* 16(16): 1280–1282. doi:10.1364/OL.16.001280.

169. Pal, S., Ozanyan, K. B., and McCann, H. (2008) A computational study of tomographic measurement of carbon monoxide at minor concentrations. *Meas. Sci. Technol.* 19: 094018 (10pp). doi:10.1088/0957-0233/19/9/094018.

170. Terzija, N., Karagiannopoulos, S., Begg, S., Wright, P., Ozanyan, K., and McCann, H. (2015) Tomographic imaging of the liquid and vapour fuel distributions in a single-cylinder direct-injection gasoline engine. *Int. J. Engine Res.* 16(4): 565–579. doi:10.1177/1468087414544178.

171. Twynstra, M. G., and Daun, K. J. (2012) Laser-absorption tomography beam arrangement optimization using resolution matrices. *Appl. Opt.* 51(29): 7059–7068. doi:10.1364/AO.51.007059.

172. Yu, T., Tian, B., and Cai, W. (2017) Development of a beam optimization method for absorption-based tomography. *Opt. Express* 25(6): 5982–5999. doi:10.1364/OE.25.005982.

173. Cai, W., Ewing, D. J., and Ma, L. (2008) Application of simulated annealing for multispectral tomography. *Comput. Phys. Commun.* 179(4): 250–255. doi:10.1016/j.cpc.2008.02.012.

174. Gillet, B., Hardalupas, Y., Kavounides, C., and Taylor, A. M. K. P. (2004) Infrared absorption for measurement of hydrocarbon concentration in fuel/air mixtures (MAST-B-LIQUID). *Appl. Therm. Eng.* 24(11–12): 1633–1653. doi:10.1016/j.applthermaleng.2003.12.005.

175. Tsekenis, S. A., and Polydorides, N. (2017) Optical access schemes for high speed and spatial resolution optical absorption tomography in energy engineering. *IEEE Sens. J.* 17(24): 8072–8080. doi:10.1109/JSEN.2017.2715364.

176. Wright, P., Ozanyan, K. B., Carey, S. J., and McCann, H. (2005) Design of high-performance photodiode receivers for optical tomography. *IEEE Sens. J.* 5(2): 281–288. doi:10.1109/JSEN.2004.841869.

177. Liu, C., Cao, Z., Lin, Y., Xu, L., and McCann, H. (2018) Online cross-sectional monitoring of a swirling flame using TDLAS tomography. *IEEE Trans. Instrum. Meas.* (99): 1–11. doi:10.1109/TIM.2018.2799098.

178. Kamimoto, T., Deguchi, Y., and Kiyota, Y. (2015) High temperature field application of two dimensional temperature measurement technology using CT tunable diode laser absorption spectroscopy. *Flow Meas. Instrum.* 46 (Part A): 51–57. doi:10.1016/j.flowmeasinst.2015.09.006.

179. Jing, W., Cao, Z., Zhang, H., Qu, Q., and Xu, L. (2017) A reconfigurable parallel data acquisition system for tunable diode laser absorption spectroscopy tomography. *IEEE Sens. J.* 17(24): 8215–8223. doi:10.1109/JSEN.2017.2652497.

180. Ma, L., and Cai, W. (2009) Tomographic imaging of temperature and chemical species based on hyperspectral absorption spectroscopy. *Opt. Express* 17(10): 8602–8613. doi:10.1364/OE.17.008602.

181. Cai, W., and Kaminski, C. F. (2014) A tomographic technique for the simultaneous imaging of temperature, chemical species, and pressure in reactive flows using absorption spectroscopy with frequency-agile lasers. *Appl. Phys. Lett.* 104(3): 034101. doi:10.1063/1.4862754.

182. Cai, W., and Kaminski, C. (2015) A numerical investigation of high-resolution multispectral absorption tomography for flow thermometry. *Appl. Phys. B-Lasers O* 119(1): 29–35. doi:10.1007/s00340-015-6012-5.

183. Ma, L., Li, X., Cai, W., Roy, S., Gord, J. R., and Sanders, S. T. (2010) Selection of multiple optimal absorption transitions for nonuniform temperature sensing. *Appl. Spectrosc.* 64(11): 1274–1282. doi:10.1366/000370210793335052.
184. Cai, W., and Kaminski, C. F. (2014) Multiplexed absorption tomography with calibration-free wavelength modulation spectroscopy. *Appl. Phys. Lett.* 104(15): 154106. doi:10.1063/1.4871976.
185. Ma, L., and Cai, W. (2008) Determination of the optimal regularization parameters in hyperspectral tomography. *Appl. Opt.* 47(23): 4186–4192. doi:10.1364/AO.47.004186.
186. Cai, W., Ewing, D. J., and Ma, L. (2011) Investigation of temperature parallel simulated annealing for optimizing continuous functions with application to hyperspectral tomography. *Appl. Math. Comput.* 217(12): 5754–5767.
187. Ma, L., Li, X., Sanders, S. T., Caswell, A. W., Roy, S., Plemmons, D. H., and Gord, J. R. (2013) 50-kHz-rate 2D imaging of temperature and H_2O concentration at the exhaust plane of a J85 engine using hyperspectral tomography. *Opt. Express* 21(1): 1152–1162. doi:10.1364/OE.21.001152.
188. Hult, J., Watt, R. S., and Kaminski, C. F. (2007) High bandwidth absorption spectroscopy with a dispersed supercontinuum source. *Opt. Express* 15(18): 11385–11395. doi:10.1364/OE.15.011385.
189. Kaminski, C. F., Watt, R. S., Elder, A. D., Frank, J. H., and Hult, J. (2008) Supercontinuum radiation for applications in chemical sensing and microscopy. *Appl. Phys. B-Lasers O* 92: 367–378. doi:10.1007/s00340-008-3132-1.
190. Niels Göran, B., Volker, E., Andreas, D., and Steven, W. (2016) Broadband fitting approach for the application of supercontinuum broadband laser absorption spectroscopy to combustion environments. *Meas. Sci. Technol.* 27(1): 015501. doi:10.1088/0957-0233/27/1/015501.
191. Qu, Q., Xu, L., Cao, Z., and Liu, C. (2016) Effects of views and spectral lines numbers on hyperspectral temperature distribution tomography. In Paper presented at 2016 IEEE International Instrumentation and Measurement Technology Conference, pp. 1–4.